A PP2A-B55 recognition signal controls substrate dephosphorylation kinetics during mitotic exit

Michael J. Cundell,[1] Lukas H. Hutter,[1]* Ricardo Nunes Bastos,[1]* Elena Poser,[1] James Holder,[1] Shabaz Mohammed,[1,2]** Bela Novak,[1]** and Francis A. Barr[1]

[1]Department of Biochemistry, University of Oxford, Oxford OX1 3QU, England, UK
[2]Department of Chemistry, University of Oxford, Oxford OX1 3TA, England, UK

PP2A-B55 is one of the major phosphatases regulating cell division. Despite its importance for temporal control during mitotic exit, how B55 substrates are recognized and differentially dephosphorylated is unclear. Using phosphoproteomics combined with kinetic modeling to extract B55-dependent rate constants, we have systematically identified B55 substrates and assigned their temporal order in mitotic exit. These substrates share a bipartite polybasic recognition determinant (BPR) flanking a Cdk1 phosphorylation site. Experiments and modeling show that dephosphorylation rate is encoded into B55 substrates, including its inhibitor ENSA, by cooperative action of basic residues within the BPR. A complementary acidic surface on B55 decodes this signal, supporting a cooperative electrostatic mechanism for substrate selection. A further level of specificity is encoded into B55 substrates because B55 displays selectivity for phosphothreonine. These simple biochemical properties, combined with feedback control of B55 activity by the phosphoserine-containing substrate/inhibitor ENSA, can help explain the temporal sequence of events during exit from mitosis.

Introduction

Integrated spatial and temporal control of numerous cellular components in mitosis is crucial to create functional daughter cells. This control is achieved through a combination of regulated proteolysis, phosphorylation, and dephosphorylation (Wurzenberger and Gerlich, 2011; Glover, 2012; Mochida and Hunt, 2012; Grallert et al., 2015). Although there has been considerable focus on understanding the regulatory networks controlling kinase and phosphatase activity (Novak et al., 2010; Ferrell, 2013), how individual substrates for the same pathway are differentially regulated is still poorly understood. It has long been known that mitotic kinases, substrates of the anaphase-promoting complex/cyclosome, and many other regulatory enzymes have specific linear recognition motifs. However, these often fail to adequately describe the behavior seen in cells, where proteins sharing similar or sometimes identical recognition determinants are regulated at widely differing rates.

Previously, we have shown that dephosphorylation and hence activation of the conserved anaphase spindle protein PRC1 is controlled by a specific protein phosphatase 2A (PP2A) holoenzyme containing a B55-family regulatory subunit (B55; Cundell et al., 2013). In addition, B55 has been implicated in reassembly of the Golgi apparatus and nuclear envelope during

mitotic exit (Schmitz et al., 2010). B55 is inhibited in mitosis by ENSA and ARPP19, two related proteins activated by phosphorylation of a serine within an inhibitory motif by the protein kinase Greatwall–MASTL (Gharbi-Ayachi et al., 2010; Mochida et al., 2010). Together, these components form the BEG (B55–ENSA–Greatwall) pathway controlling mitotic exit (Cundell et al., 2013). Because Cdk1/cyclin B activates Greatwall–MASTL, B55 inhibition is maintained until cyclin B is degraded (Castilho et al., 2009; Gharbi-Ayachi et al., 2010; Mochida et al., 2010; Rangone et al., 2011). Once all chromosomes have aligned and are under tension on the metaphase spindle, the anaphase-promoting complex triggers destruction of cyclin B and the separase inhibitor securin. Separase activation and chromosome separation and segregation then rapidly follow. Greatwall is inactivated by protein phosphatase 1 (PP1) reducing the production of phosphorylated ENSA (Heim et al., 2015). Initially, B55 remains inhibited because ENSA is present in excess and only slowly dephosphorylated (Williams et al., 2014). Because ENSA binds B55 tightly and shows apparent slow zero-order dephosphorylation kinetics, it has been referred to as an unfair substrate crowding out other substrate proteins (Williams et al., 2014). This creates a delay in dephosphorylation of PRC1 and, hence, anaphase spindle assembly and cytokinesis only commence once chromosomes have become segregated

---

*L.H. Hutter and R.N. Bastos contributed equally to this paper.

**S. Mohammed and B. Novak contributed equally to this paper.

Correspondence to Francis A. Barr: francis.barr@bioch.ox.ac.uk

Abbreviations used: BEG, B55–ENSA–Greatwall; BPR, bipartite polybasic recognition determinant; BR, basic residue; FG, phenylalanine-glycine; IBB, importin-β binding; PPSIM, protein phosphatase simulation model.

(Cundell et al., 2013). Removal of the ENSA–Greatwall inhibitory system results in constitutive B55 activity, causing mitotic catastrophe and a cut phenotype because of precocious central spindle formation and cytokinesis (Manchado et al., 2010; Voets and Wolthuis, 2010; Cundell et al., 2013).

Despite this central role of the BEG pathway in mitotic exit, few substrates are known and the mode of substrate recognition by B55 is not well understood. The best understood B55 substrate in mitosis is GM130, a Golgi tethering protein and Cdk1/cyclin B substrate required for ER–Golgi traffic and Golgi structure (Lowe et al., 2000); however, the specific recognition sequences in GM130 were not defined. Analysis of the structure of B55 showed that an acidic substrate-binding groove on the regulatory subunit is important for dephosphorylation of the basic substrate protein tau (Xu et al., 2008); however, this has not been explored more generally. Here, we carry out a global identification of B55 substrates in mitosis, identify a general B55 substrate recognition determinant, and explain how its properties dictate the rate at which substrates are dephosphorylated by this pathway during mitotic exit.

Results

B55 substrates share a unique anaphase signature

To identify B55 substrates, the unique features of its Greatwall–MASTL ENSA regulatory pathway were exploited. These sites should show delayed sigmoidal dephosphorylation kinetics, which are slowed when B55 activity is reduced, and are accelerated to an exponential decay when the B55 inhibitor pathway is inactivated by removal or either Greatwall–MASTL or ENSA (Fig. 1 A; Cundell et al., 2013). In contrast, substrates of other phosphatases or sites that are not dephosphorylated will show different temporal profiles and be unaltered by these conditions. Whole-cell extracts from phosphatase-active control, B55 depleted phosphatase-inactive, or Greatwall–MASTL depleted inhibitor-inactive states were incubated for up to 45 min to allow substrate dephosphorylation. Western blotting confirmed efficient depletion of phosphatase subunits and Greatwall–MASTL under these conditions (Fig. S1, A and B). The samples were then separated into soluble and chromatin fractions and subjected to in-solution tryptic digestion followed by dimethyl labeling and phosphopeptide enrichment steps before reverse-phase online liquid chromatography (LC) mass spectrometry (Fig. S1 C). Phosphopeptides in the different conditions were identified and filtered using MaxQuant software (Cox et al., 2011) to generate a dataset in which >23,000 phosphorylation sites are quantitated over time for each condition (Table S1). Comparison of Western blotting data (Fig. 1 B) with the mass spectrometry dataset shows that the known Cdk1 site on PRC1 at pT481 was identified and quantitated by this global temporal phosphoproteomics approach (Fig. 1 C).

Because B55 activity is not constant as a function of time in this system, it is not possible to accurately extract dephosphorylation rates directly from the kinetic data. To circumvent this issue, we developed a protein phosphatase simulation model (PPSIM) for substrate dephosphorylation under control, B55, and Greatwall–MASTL–depleted conditions. In this model, substrate dephosphorylation can occur either by an ENSA-regulated B55 component or by B55-independent activity (Fig. 1 D). Using the mass spectrometry data, the software calculated B55

activity as a function of time from the amount of phosphorylated ENSA in the system and relative phosphopeptide abundance for the initial starting conditions (Fig. 1 E). This constrained model accurately describes dephosphorylation of the model B55 substrate PRC1 pT481 k_{b55} = 0.121 min^{-1} (Fig. 1 F) and was able to fit B55-dependent and -independent dephosphorylation rates and calculate relative abundance for a further 7,390 phosphopeptides (Table S2). Of these, 2,960 showed a B55-dependent rate constant >0 (Fig. S1 D). High-confidence B55 substrates were defined as the top 15th percentile in terms of rate where the mean square deviation between the model output and experimental data were below 0.005 (Fig. 1 G and Table S3). This list includes the previously identified B55 substrates PRC1 pT481 and Cdc20 pS41 (Mochida et al., 2010; Cundell et al., 2013; Williams et al., 2014). A further site on PRC1 at pT470 k_{b55} = 0.214 min^{-1} (Fig. 1 H), in addition to sites on mitotic spindle proteins were identified, including the Aurora A regulator TPX2 at pT369 k_{b55} = 0.208 min^{-1} (Fig. 1 I) and nuclear pore proteins (Fig. 1 G). Importantly, dephosphorylation kinetics showed the expected dependency on B55 and Greatwall–MASTL. Likewise, the top 15th percentile of the 3,000 phosphopeptides with a B55-independent rate constant >0 (Table S2) were defined as high-confidence B55-independent substrates (Fig. 1 J and Table S4). These include several mitotically regulated chromosome proteins, including the chromosome passenger protein borealin/CDCA8 (Fig. 1 K) and the chromokinesin KIF4A (Fig. 1 L). For these substrates, dephosphorylation kinetics is unaltered by depletion of B55 or Greatwall–MASTL.

Identification of a bipartite polybasic recognition determinant for B55

To ask if there is a common feature shared by B55 substrates, enrichment or exclusion of the different amino acids relative to our total dataset of mitotic phosphopeptide sequences was calculated with IceLogo (Colaert et al., 2009). This revealed that B55 substrates share a bipartite positive-charged polybasic motif surrounding a central consensus Cdk site with an enrichment of phosphothreonine (Fig. 2 A). These features are absent from the experimentally determined conserved Cdk1-consensus motif (Alexander et al., 2011), supporting the idea that they relate to dephosphorylation by B55 rather than phosphorylation by Cdk1. For candidate B55 substrates, the phosphorylated amino acid frequency is 45% phosphothreonine (pT) and 55% phosphoserine (pS; Table S3) compared with 25% pT, 73% pS, and <2% phosphotyrosine (pY) for the total phosphoproteome (Table S1). Acidic residues aspartate and glutamate are excluded both within and downstream of the phosphorylation site. B55-independent substrates show a different pattern with enrichment of two basic residues (BRs) upstream of the phosphorylated residue (Fig. 2 B), similar to the Aurora kinase consensus motif (Alexander et al., 2011; Kettenbach et al., 2011). Further examples can be visualized for both B55-dependent and -independent substrates online (http://cellcycle.org.uk/static/PPSIM/timecourse.html).

Further analysis revealed that B55-dependent dephosphorylation rate for all peptides with k_{b55} > 0 exhibits a nonlinear relationship with net charge that can be fitted with a reciprocal exponential curve (Fig. 2 C). The most rapidly dephosphorylated substrates are most basic (1–200), and those in the slowest category the least basic (1,000–2,500; Fig. 2 C). In contrast, neither B55-dependent nor B55-independent dephosphorylation rates show any obvious relationship with
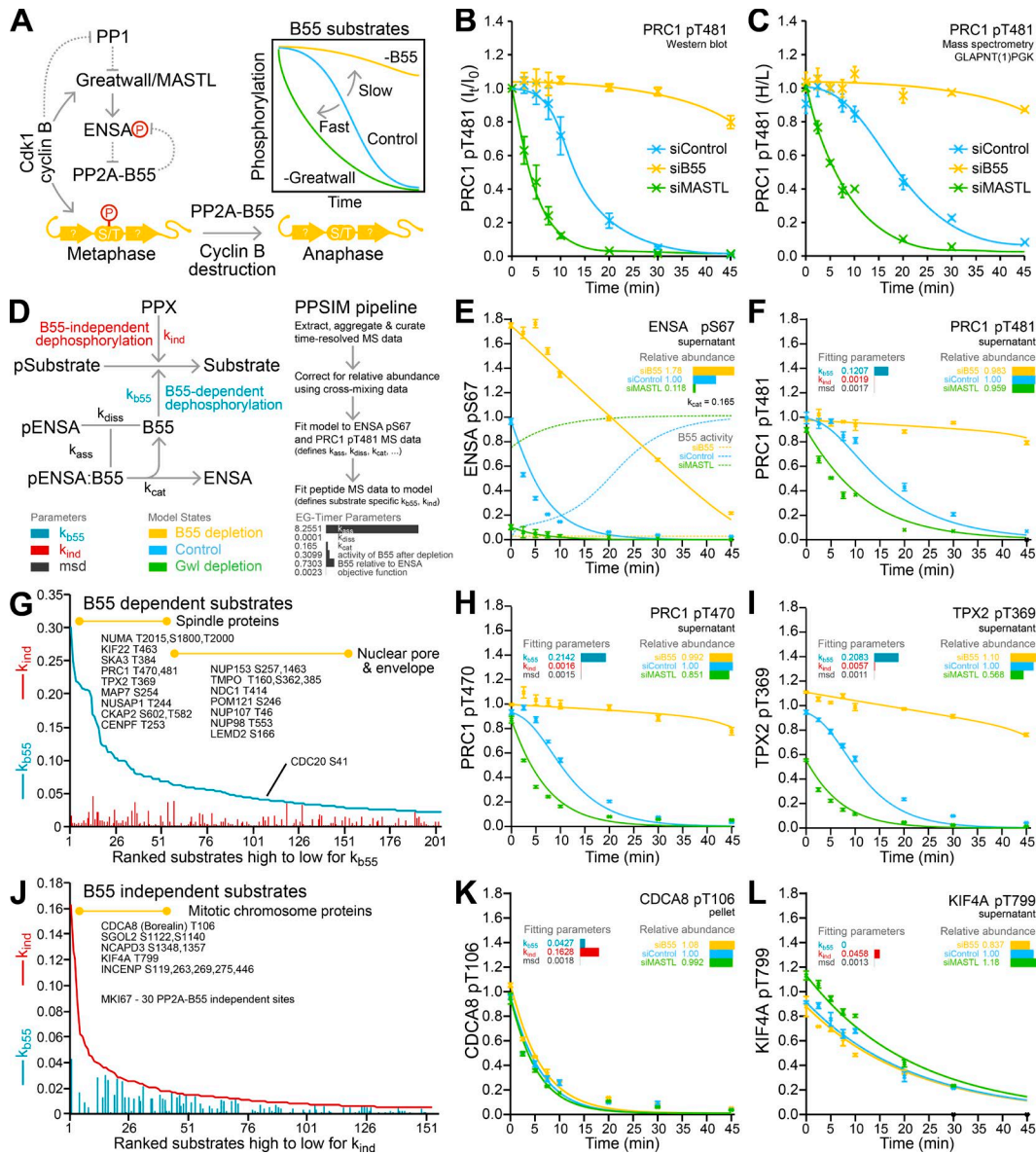
Figure 1. **B55 substrates share a unique temporal signature.** (A) A schematic of the BEG pathway showing regulation of generic Cdk1 substrates at the metaphase to anaphase transition. Idealized temporal dephosphorylation profiles for B55 substrates in control (Control), B55 (-B55), and Greatwall–MASTL (-Gwl) inactivated conditions are shown in the graph. (B) Western blot analysis of PRC1 pT481 dephosphorylation in control (siControl), B55 (siB55)-depleted, and Greatwall–MASTL (siMASTL)–depleted cell extracts. PRC1 pT481 level as a function of time expressed as integrated signal (I_t)/integrated signal at $t = 0$ (I_0), error bars indicate the SEM ($n = 3$ independent experiments). Time was measured from the point at which lysis buffer was added to cells to termination of phosphoprotein phosphatase–dependent dephosphorylation by addition of okadaic acid. (C) Heavy/light (H/L) ratios were extracted from whole-cell phosphoproteome mass spectrometry data for PRC1 pT481. (D) The wiring diagram used in the mathematical model to describe substrate dephosphorylation by B55-dependent and independent pathways is shown. PPSIM software created for this study fits time-resolved mass spectrometry data to this kinetic model allowing for three states: control, B55 depletion, and MASTL–Greatwall depletion. Depletion levels and behavior of ENSA and PRC1 pT481 as a model substrate for this pathway are used to parameterize and constrain the model. The key outputs for each substrate are B55-dependent (k_{b55}) and independent (k_{ind}) rates, a quality-of-fit parameter (mean square deviation from the mean [msd]), and relative abundance at steady state extracted from cross-mixing of $t = 0$. A detailed description is provided in the online supplement. (E) ENSA dephosphorylation, H/L ratio, adjusted for relative abundance at $t = 0$ for control, B55-depleted, and MASTL-depleted conditions. Curves show the PPSIM model output. Because ENSA has a unique place in the model as both a substrate and inhibitor of B55, the rate constant (k_{cat}) is used to describe the pool of B55 activity available for all other substrates as a function of time. (F) PPSIM output for PRC1 pT481 showing the rate of B55-dependent (blue) and independent (red) dephosphorylation and relative abundance for the same data in panel C. (G) High-confidence B55-dependent substrates ranked by k_{b55}, k_{ind} for each substrate is also shown. Major classes of substrate protein involved in mitotic spindle regulation and nuclear pore/envelope formation, and the known B55 substrate Cdc20 pS41, are listed. The yellow bar marks the ranges in which these factors were found. (H and I) PPSIM plots for two B55 substrates with high $k_{b55} > 0.2$, PRC1 pT470 (H) and TPX2 pT369 (I), are shown. (J) High-confidence B55-independent substrates ranked by k_{ind}, k_{b55} for each substrate is also shown. Major classes of substrate protein involved in regulation of chromosomes in mitosis are listed. The yellow bar marks the ranges in which these factors were found. (K and L) PPSIM plots for two B55-independent substrates with high k_{ind}, CDCA8 pT106 (K) and KIF4A pT799 (L), are shown. Error bars indicate the SEM (siControl $n = 5$, siB55 $n = 3$, siMASTL $n = 2$) for all mass spectrometry data and PPSIM outputs.
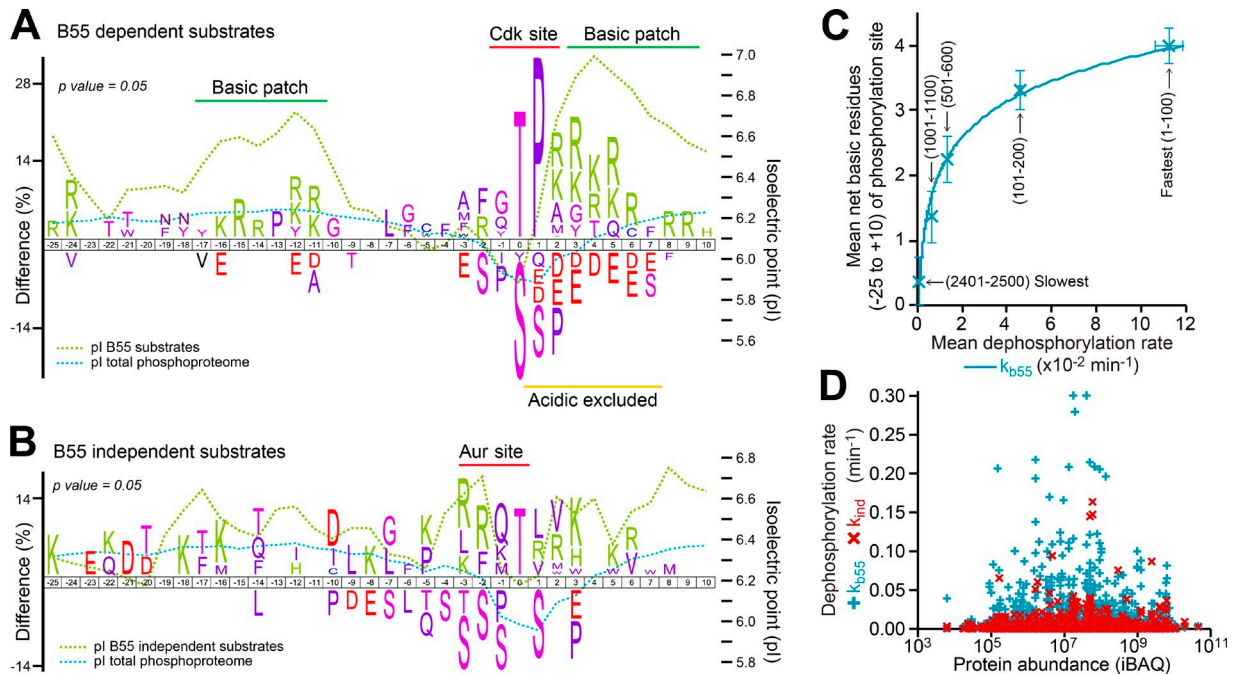
Figure 2. **B55 substrates contain a bipartite polybasic motif.** (A) A 36–amino acid sequence centered on the phosphorylated residue for the high-confidence B55-dependent (203 peptides) and (B) -independent (153 peptides) substrates was compared against the experimentally determined total cell phosphoproteome data (23,131 peptides) using IceLogo with P = 0.05. Plots for substrate enriched and excluded amino acids and average isoelectric point (pI, green dotted line) and the total cell phosphoproteome (blue dotted line) within this sequence window are shown. (C) Mean B55-dependent dephosphorylation rates for the fastest (1–100) and progressively slower groups of ranked substrates as a function of the mean number of net basic residues. Error bars indicate the SEM (n = 100) for the different ranked groups of substrates. (D) Initial B55-dependent (blue, +) and independent (red, x) dephosphorylation rates for the top 2,960 peptides ranked by k_{b55} as a function of protein abundance calculated using intensity based absolute quantification (iBAQ) from a total mitotic cell proteome dataset.

protein abundance calculated from a total mitotic cell proteome (Fig. 2 D and Table S5). These findings suggested that B55 may select substrates by electrostatic properties and that dephosphorylation rate may be encoded by net basic charge for substrates with widely differing abundance.

Dephosphorylation rate is encoded by a cooperative electrostatic signal

To evaluate this hypothesis, PRC1 was used as a model substrate containing a B55 bipartite polybasic recognition determinant (BPR; Fig. 3 A). A role for the conserved D- and KEN-boxes, which regulate PRC1 stability, in B55 recognition was excluded, because proteins with point mutations in these motifs behaved as the wild-type protein (Fig. S2, A–C) and showed normal anaphase spindle recruitment (Fig. S2 D). Deletion mapping experiments confirmed that a region containing the B55 BPR and spectrin-fold domain has dephosphorylation kinetics similar to the full-length protein (Fig. S2, A–C) but fails to target to microtubules in anaphase (Fig. S2 D). Shorter truncations showed rapid unregulated dephosphorylation within 2.5 min in cell extracts (Fig. S2, B and C). This indicates that phosphatases other than B55 can now act on these truncated substrates, which therefore can not be used for further analysis of specificity or function. To directly test the role of charge in determining dephosphorylation rate, a graded series of full-length PRC1 substrates with progressively less basic character was created by mutating the four patches comprising the B55 BPR (Fig. 3 A). Progressive removal of BRs resulted in reduced dephosphorylation rate at T481 (Fig. 3, B and C) and T470 (Fig. 3 D). The initial dephosphorylation rate (V_{dp}) of PRC1

mutants is a sigmoid function of the number of BRs within the BPR (Fig. 3 E, observed rate) with a sharp threshold around a value of four. Ultrasensitive dependence of V_{dp} on the number of BRs is a hallmark of cooperative action by the salt bridges. To explain this, we propose that BRs increase the affinity of the substrate for the enzyme through electrostatic interactions (salt bridges). Such interactions extend the residence time of good substrates on the enzyme, increasing the probability of the dephosphorylation reaction. Formulating this idea within the framework of Michaelis–Menten enzyme kinetics generates a rate expression identical to the logistic equation that defines a sigmoid function (see analysis of electrostatic properties of B55 substrates in Materials and methods). In this instance, cooperativity among salt bridges mediating the enzyme–substrate interaction creates an exponential increase in the substrate residence time and sigmoid dependence of the initial rate on BR that fits well with experimental data (Fig. 3 E, theoretical, solid curve). This results in differential dephosphorylation kinetics as a function of BR (Fig. 3 F), a relationship that can explain the range of temporal control seen for B55 substrates during mitotic exit.

B55 BPR sets the time of PRC1 activation in mitotic exit

Timely anaphase spindle recruitment of PRC1 requires B55-mediated dephosphorylation of the two Cdk1 sites close to the microtubule-binding domain (Cundell et al., 2013). Modulation of the B55 BPR should thus alter this timing. To test this prediction, we studied two PRC1 BPR mutants, mutant 11, retaining two BRs, or mutant 12, lacking all BRs. Compared with wild-type PRC1, mutant 11 and 12 exhibited intermediate
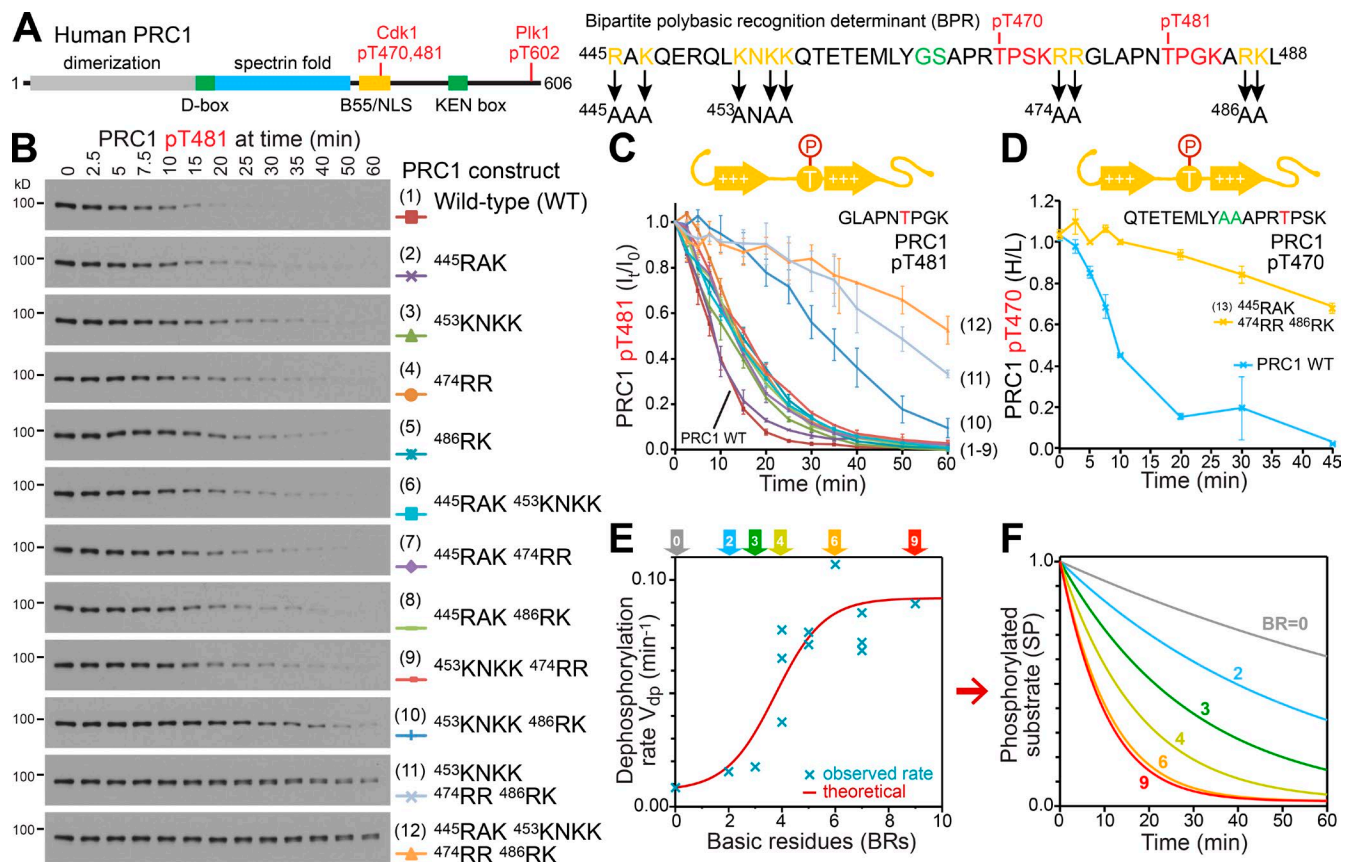
Figure 3. **Dephosphorylation rate of B55 substrates is encoded by BPR.** (A) A schematic of human PRC1 based on structural data (Subramanian et al., 2010, 2013) with phosphorylation sites for Cdk1 and Plk1 (Neef et al., 2007), D- and KEN-box destruction motifs, and a putative NLS. Alanine-scanning mutations were introduced at basic residues (BRs) in B55 BPR and putative NLS region as marked in the sequence below the schematic. BRs within the consensus Cdk1-phosphorylation sites (red) were not mutated, since this compromises phosphorylation. To allow analysis of T470 dephosphorylation, the GS sequence (green) at position 465/466 was mutated to AA, creating a unique peptide that could be differentiated from the endogenous protein by mass spectrometry. (B) PRC1 pT481 Cdk1-site dephosphorylation of GFP-tagged wild-type PRC1 (1) and the series of single and combined basic patch mutants (2–12) was followed by Western blotting. (C) PRC1 pT481 dephosphorylation for all samples numbered as in B; error bars indicate SEM (n = 3 independent experiments). (D) PRC1 pT470 dephosphorylation profiles for the endogenous wild-type and BPR/GS mutant PRC1 extracted from mass spectrometry data; error bars indicate SEM (n = 2). (E) The effect of BRs within the BPR on the dephosphorylation of PRC1 mutants described in B and C. Initial rate versus BR. Experimental data (observed rate, blue x) and kinetic equation (solid curve, red). (F) Numerical simulations of dephosphorylation kinetics with representative BR values.

or greatly slowed dephosphorylation kinetics (Fig. 3, B and C), respectively. In G2 cells, wild-type PRC1 was nuclear, as expected, and recruitment to microtubules commenced by 4 min of anaphase (Fig. 4 A). PRC1 mutants 11 and 12 showed delayed and attenuated recruitment to the central spindle from 8 and 14 min, respectively (Fig. 4, B–D), confirming that dephosphorylation underpins timely activation of PRC1. Importantly, all basic patch mutant PRC1 proteins localized to microtubules in interphase cells (Fig. S2 E), excluding the possibility that mutation within the polybasic region simply abolished microtubule binding. These results also reveal an interesting relationship between the PRC1 BPR and NLSs. Both mutants 11 and 12 failed to localize to the nucleus in G2 cells since [474]RR and [486]RK form part of the PRC1 NLS (Fig. S2 E). Other residues within the B55 BPR are not required for nuclear import (Fig. S2 E), indicating that although the B55 BPR and NLS overlap, they are separable motifs with discrete functions.

To generalize the idea that modulation of a B55 BPR alters the timing of substrate regulation in anaphase, the newly identified B55 substrate and spindle assembly factor TPX2 was investigated. TPX2 contains a BPR flanking a Cdk site at T369

adjacent to an importin-α binding domain (Schatz et al., 2003; Fig. S3 A). Removal of the BRs within the TPX2 BPR reduced the rate of pT369 dephosphorylation >20-fold (Fig. 4 E) and also altered the regulation of TPX2 in anaphase. Instead of becoming recruited to the central spindle between 6 and 8 min of anaphase shortly after PRC1 (Figs. 4 F and S3 B), the TPX2 BPR mutant was recruited directly into the nucleus in telophase, 16–20 min after anaphase onset (Figs. 4 G and S3 C). Failure to dephosphorylate TPX2 in anaphase and release importin-α therefore leads to aberrant nuclear import rather than anaphase spindle and midbody targeting (Wittmann et al., 2000).

In summary, B55-mediated dephosphorylation rates of PRC1 and TPX2, and their timely recruitment to the anaphase spindle, are dependent on the properties of their respective BPR sequences.

Substrate selection by an acidic surface on the B55 regulatory subunit

Having delineated a key feature of substrates, we next turned to B55 to define the recognition determinant on the enzyme. Our previous biochemical data show this must lie within the unique
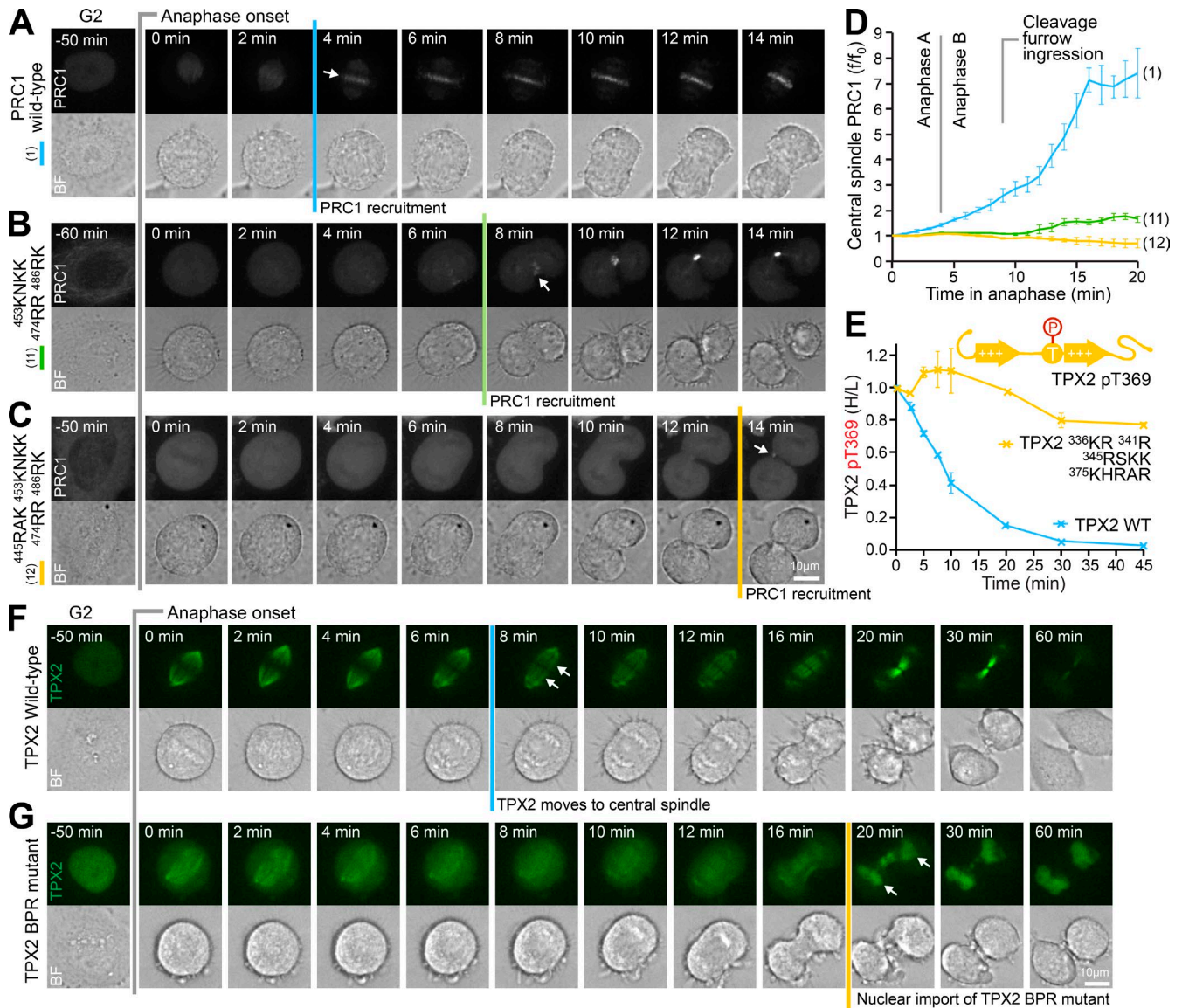
Figure 4. BPRs encode timely dephosphorylation of B55 substrates. (A) HeLa cells depleted of endogenous PRC1 using siRNA directed to the 3′ UTR were transfected with GFP-tagged wild-type, mutant 11 (B), and mutant 12 PRC1 (C) as indicated. These cells were imaged every minute passing from G2 through mitosis and into anaphase. A single image in G2 before mitotic entry is shown to demonstrate nuclear localization in the control condition. A series of maximum intensity projected images from 0 to 14 min taken every 2 min from anaphase onset ($t = 0$) is shown. Anaphase onset was defined using the brightfield images in which the aligned metaphase plate and initial time of chromosome segregation can be visualized. The onset of anaphase ($t = 0$ min) was set as the time point preceding the first frame in which chromosome segregation was visible. Arrows indicate the initiation of PRC1 recruitment to the spindle midzone. (D) PRC1 levels at the spindle midzone expressed as integrated fluorescence (f)/integrated fluorescence at $t = 0$ (f_0); error bars indicate the SEM ($n = 6$–8). Times of anaphase A, anaphase B, and cleavage furrow ingression for control cells are marked. Constructs are numbered as in Fig. 3 B. (E) TPX2 pT369 Cdk1-site dephosphorylation of GFP-tagged wild-type (WT) TPX2 and the B55 BPR mutant was followed by mass spectrometry. Mean heavy/light (H/L) ratios were extracted from mass spectrometry data. Error bars indicate the SEM ($n = 3$). (F and G) GFP-TPX2 (F) or the TPX2 BPR mutant (G) were imaged every minute passing from G2 through mitosis and into anaphase. A single image in G2 before mitotic and a series of maximum intensity projected images from 0 to 14 min taken every 2 min from anaphase onset ($t = 0$) are shown. Arrows indicate the initiation of TPX2 recruitment to the central spindle region and import of the TPX2 BPR mutant into the nucleus in telophase.

B55 regulatory subunit for substrates such as PRC1 (Cundell et al., 2013). B55 has 10 conserved acidic residues forming an extended surface on its seven-bladed β-propeller regulatory subunit, adjacent to the active site in the catalytic subunit (Fig. S4 A; Xu et al., 2008). Parts of this acidic surface contribute to recognition of the basic B55 substrate protein tau (Xu et al., 2008). This agrees with the proposed electrostatic mechanism for substrate recognition, where the bipartite polybasic region in the substrate interacts with an acidic surface on the enzyme. To test if this acidic surface is important for specific substrate

recognition, 10 acidic residues in the B55α phosphatase regulatory subunit were mutated to alanine to create the corresponding DE/A mutant. Incorporation of this mutant regulatory subunit into B55 holoenzyme complexes was unaltered (Fig. S4 B), and their activity toward model substrates was therefore tested. Comparison of DE/A mutant and wild-type enzymes revealed that loss of the B55α acidic surface greatly reduced activity toward Cdk1/cyclin B–phosphorylated PRC1 pT481 (Fig. 5 A). As expected, a different subclass of PP2A, B56γ, was not able to dephosphorylate PRC1 pT481 (Fig. 5 A), showing enzyme
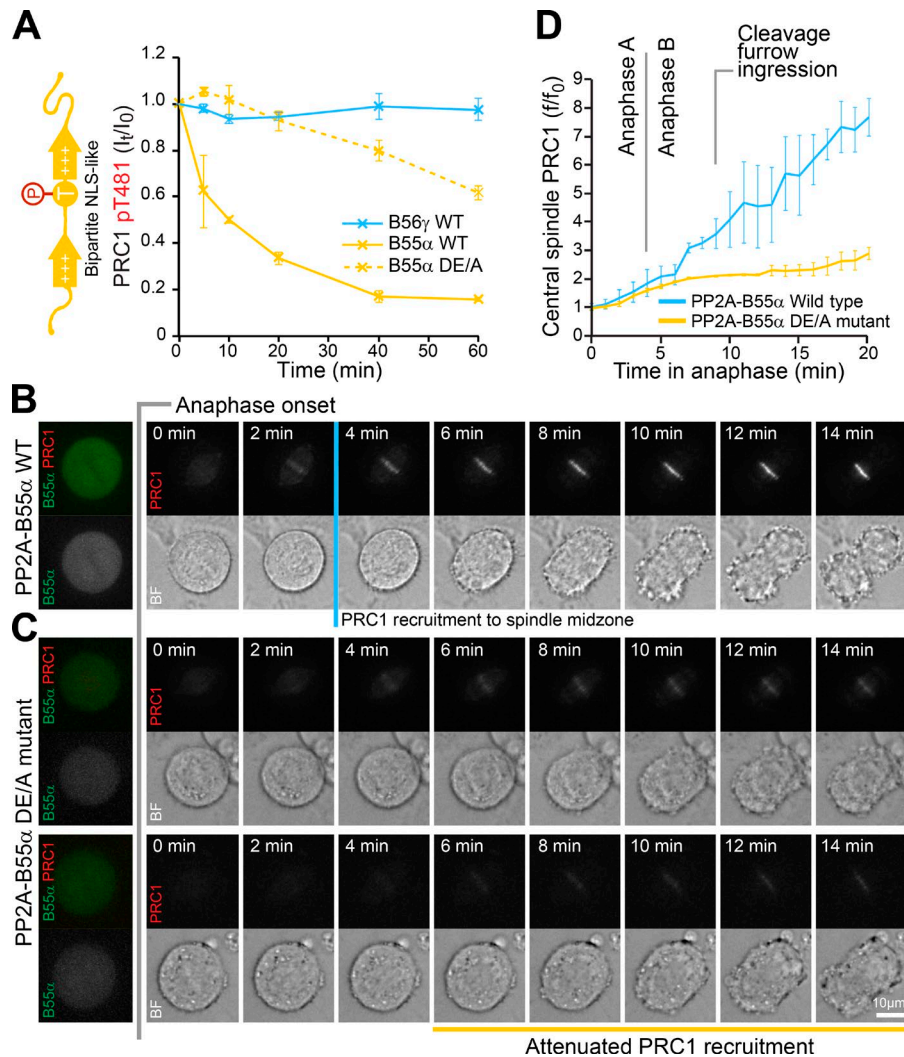
Figure 5. **A complementary acidic surface on the B55 regulatory subunit is required for efficient dephosphorylation and timely activation of PRC1.** (A) Dephosphorylation of Cdk-phosphorylated PRC1 at pT481 by B55, B55α DE/A, or B56γ was followed by Western blotting; error bars indicate the SEM ($n = 3$). (B) Hela cells depleted of endogenous B55 regulatory subunits using siRNA directed to the 3′ UTR were transfected with GFP-tagged B55α WT regulatory subunit or (C) the B55α DE/A mutant and mCherry-tagged wild-type PRC1. These cells were imaged every minute passing from G2 through mitosis and into anaphase. A single image of GFP-B55α in G2 before mitotic entry is shown to demonstrate expression of the phosphatase regulatory subunit. A series of maximum intensity projected images from 0 to 14 min taken every 2 min from anaphase onset ($t = 0$) is shown for PRC1. Two representative sets of images are shown for the B55α DE/A mutant–expressing cells. (D) PRC1 levels at the spindle midzone. Error bars indicate the SEM ($n = 3$). Times of anaphase A, anaphase B, and cleavage furrow ingression for control cells are marked. WT, wild type.

specificity is maintained under these conditions. These data show that the extended acidic face of B55α is important for recognition of bipartite polybasic substrates.

The importance of the B55 acidic surface for temporal regulation of mitotic exit was investigated using the activation of PRC1 at the anaphase spindle. In mitotic cells expressing wild-type B55α, PRC1 recruitment to microtubules commenced by 4 min of anaphase (Fig. 5 B), as expected. In cells expressing the B55α DE/A mutant, PRC1 showed delayed and attenuated recruitment to the spindle midzone in anaphase (Fig. 5, C and D). The altered timing of anaphase recruitment and effect on dephosphorylation rate seen with the B55α DE/A mutant was comparable to that seen with PRC1 BPR mutant 12 (Fig. 3, A–C). The acidic, substrate-complementary surface of B55 is therefore important for timing PRC1 activation during mitotic exit.

The B55 inhibitor and unfair substrate ENSA has a BPR

We next sought to understand if these properties are relevant for the B55 regulator ENSA. ENSA occupies a unique position in the BEG pathway as both an inhibitor and a substrate for B55. It has a B55 BPR flanking the conserved ENSA motif containing the S67 residue phosphorylated by Greatwall–MASTL (Fig. 6 A). Mutation of the conserved aromatic and acidic residues in this motif resulted in reduced or abolished

phosphorylation by Greatwall (Fig. 6 B), defining a recognition motif for this kinase. Intriguingly, considering the enrichment of phosphothreonine in B55 substrates (Fig. 2 A), no detectable phosphorylation of the ENSA S67T mutant was seen (Fig. 6 B), suggesting that Greatwall was unable to phosphorylate it. Mutations in the B55 BPR of ENSA did not reduce Greatwall phosphorylation, and these could be analyzed further. To directly test the role of charge in determining dephosphorylation rate, a graded series of full-length ENSA substrates with progressively less basic character was created by mutating the four patches comprising the B55 BPR. In addition, the conserved tyrosine 64 in the ENSA motif was mutated. Progressive removal of BRs resulted in reduced dephosphorylation rate (Fig. 6, C and D). A further reduction in rate was observed when Y64 was mutated, suggesting this plays a role in binding to B55. This is in agreement with previous work showing that this residue can be cross-linked to the B55 catalytic and regulatory subunits (Mochida, 2014). The initial dephosphorylation rate (V_{dp}) of ENSA mutants is a sigmoid function of the number of BRs within the BPR with a sharp threshold around BR value of 6 (Fig. 6 E, observed rate), compared with 4 for the substrate PRC1 (Fig. 3 E). This agrees with the idea that the electrostatic interactions would need to increase the residence time of an inhibitor, ENSA, on the enzyme above that of good substrates such as PRC1 or TPX2. As in the case of substrates, this can be
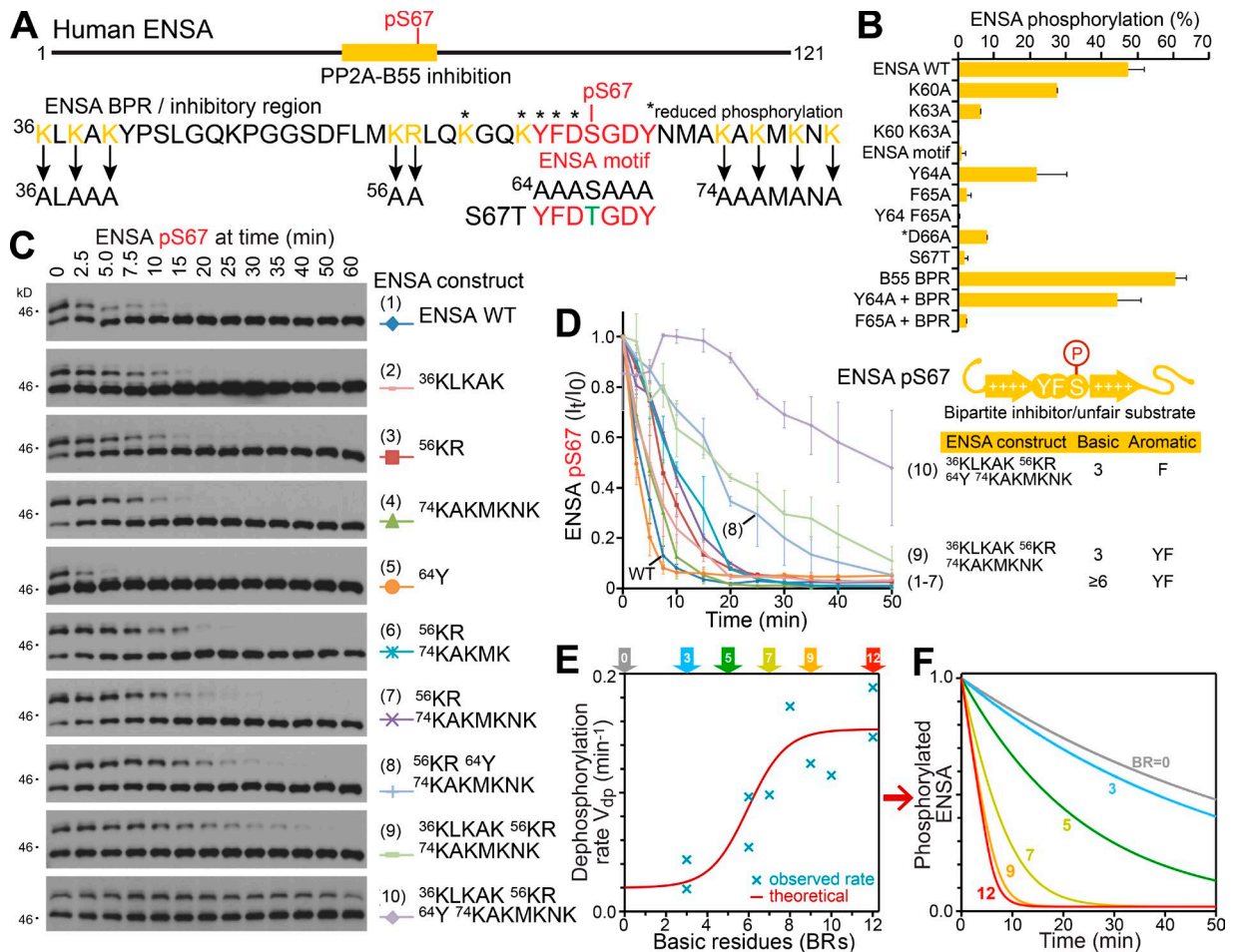
Figure 6. **A BPR directs dephosphorylation of the B55 inhibitor ENSA.** (A) A schematic of the B55 inhibitory region of human ENSA with the Greatwall–MASTL phosphorylated S67 highlighted in red. Alanine-scanning mutations were introduced at basic residues (BRs) in the three basic patches making up the B55 BPR and conserved residues in the ENSA motif as marked in the sequence. (B) Steady-state levels of ENSA phosphorylation in mitotic cells; error bars indicate the SEM ($n \geq 2$). (C) ENSA pS67 Greatwall-site dephosphorylation of GFP-tagged wild-type (WT) ENSA (1) and the series of single and combined basic patch mutants (2–10) was followed by Western blotting of Phostag gels. (D) ENSA pS67 dephosphorylation, numbered as in C; error bars indicate the SEM ($n \geq 2$). (E) The effect of BRs within the BPR on the dephosphorylation of ENSA mutants described in C and D. Initial rate versus BR. Experimental data (observed rate, blue x) and kinetic equation (solid curve, red). (F) Numerical simulations of dephosphorylation kinetics with representative BR values.

explained within the framework of classical enzyme kinetics, because cooperativity among salt bridges results in an exponential increase in inhibitor residence time and creates a sigmoid dependence of the initial rate (Fig. 6 E, theoretical, solid curve) and differential dephosphorylation kinetics on BRs (Fig. 6 F). This model provides a simple explanation unifying the behavior of both substrates and the inhibitor or unfair substrate ENSA, because both are governed by the same properties. ENSA occupies a more extreme position in the system with respect to basic charge and has additional interactions with the catalytic subunit via aromatic residues in the ENSA motif.

Phospho–amino acid selectivity of B55

One feature of B55 substrates not obviously explained by the proposed electrostatic selection mechanism is the enrichment for phosphothreonine versus phosphoserine when compared with the total phosphoproteome (Fig. 2 A). To explore this further, the phosphorylated threonine residues in PRC1 and TPX2 were converted to serine. Remarkably, these mutant proteins although phosphorylated were dephosphorylated far less rapidly than the wild-type proteins (Fig. 7, A

and B). An additional feature of substrates must therefore be important for efficient recognition of phosphoserine. Some B55 substrates, including ENSA, contain aromatic or bulky hydrophobic and acidic residues immediately upstream of the phosphorylation sites. Introduction of the upstream aromatic/acid motif from ENSA into PRC1 S470/481, but not the acidic residue alone, created a substrate with dephosphorylation kinetics indistinguishable from wild-type PRC1 T470/481 (Fig. 7 C). It is intriguing that aromatic residues are important for phosphoserine containing substrate recognition in this assay because this is reminiscent of cyclic peptide–like inhibitors of PP2A, which interact directly with the PP2A catalytic subunit in part via an aromatic residue occupying a pocket close to the catalytic center (Xu et al., 2008). Although the precise mode of ENSA binding to B55 is not yet known, these findings provide a plausible mechanism involving the BPR and additional aromatic residues.

These results show that both charge and choice of serine or threonine can affect the B55-dependent dephosphorylation rate. Together, this may explain why the phosphoserine containing unfair substrate ENSA acts as a potent B55 inhibitor.
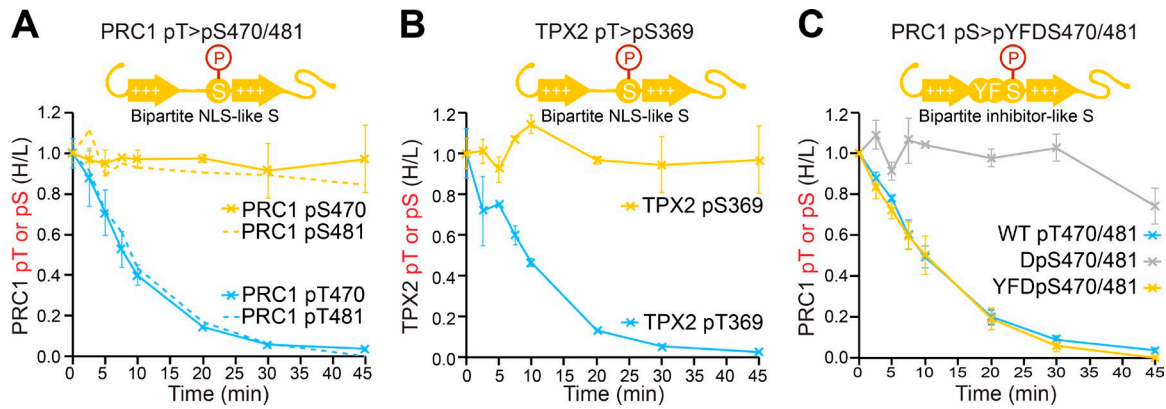
Figure 7. **Phospho–amino acid selectivity of B55 has implication for substrates and the B55 inhibitor ENSA.** (A) Dephosphorylation of wild-type PRC1 at T470 and T480 was compared with S470 and S481 mutants using mass spectrometry. Heavy/light (H/L) ratios were extracted from mass spectrometry data for all peptides; error bars show the SEM (n = 2). (B) Dephosphorylation of wild-type TPX2 at T369 was compared with a S369 mutant using mass spectrometry. H/L ratios were extracted from mass spectrometry data for all peptides; error bars show the SEM (n = 2). (C) Dephosphorylation of wild-type (WT) T470/T481 PRC1 was compared with inhibitor (ENSA-like) DS470/DS481 and YFDS470/YFDS481 mutants using mass spectrometry. H/L ratios were extracted from mass spectrometry data for all peptides; error bars show the SEM (n = 6 wild-type control and n = 3 mutants).

B55 regulates timing of nuclear pore formation and function in mitotic exit

Finally, we asked if the combined action of the ENSA–Greatwall regulatory system and BPR sequences in substrate proteins provides a general mechanism explaining the order of B55-dependent processes in mitotic exit. For cell division to succeed, it is crucial that nuclear pore formation and resumption of nuclear import occurs only after the chromosomes have been segregated (Wandke and Kutay, 2013). Our mass spectrometry dataset shows that B55-dependent dephosphorylation of mitotic and anaphase spindle proteins is followed by nuclear pore and envelope proteins in vitro (Fig. 1 G), fitting with the order of these processes in unperturbed cells exiting mitosis. To provide further evidence that the ENSA–Greatwall regulatory system and BPR sequences in substrate proteins explain the in vivo behavior, nuclear pore formation and function were followed using the candidate phosphoserine-containing B55 substrate NUP153.

Proteomic data show NUP153 dephosphorylation in vitro is ~7.5 min later (Fig. 8 A, solid lines) than that of the fastest substrates such as TPX2 and PRC1 (Fig. 8 A, dotted line). Fitting with these in vitro dephosphorylation kinetics, NUP153, phenylalanine-glycine (FG) repeat nucleoporins and RanBP2 identified as candidate B55 substrates are only recruited to the forming nuclear membrane surrounding the chromatin in telophase (Fig. 8 B and Fig. S5 A). In agreement with this late timing k_{b55} is <0.1 for this class of substrate, under half the values seen for the fastest substrates such as PRC1 and TPX2 which become active in anaphase. The delayed recruitment of NUP153, FG-repeat nucleoporins and RanBP2 was abolished in Greatwall–MASTL–depleted cells, which showed precocious localization of these factors to anaphase chromatin (Figs. 8 B and S5 A). Conversely, depletion of B55 delayed recruitment of these same factors so they were absent from the nuclear membrane surrounding the chromatin in telophase (Figs. 8 B and S5 A). Nuclear envelope proteins such as the lamin B receptor and AHCTF/ELYS (AT-hook transcription factor), the most upstream component of the nuclear pore assembly pathway, are already present in anaphase cells, and timing of their recruitment was not altered under the same conditions (Fig. S5, B and C), suggesting they are regulated by other phosphatases (Vagnarelli et al., 2011; Qian et al., 2015).

To test when nuclear import resumes if the B55 pathway is perturbed, cells expressing GFP-tagged NUP153 and the mCherry-tagged importin-β binding domain (IBB) of importin-α were imaged. In control cells, nuclear pore recruitment commences at 8–9min of anaphase onset (Fig. 8, C and D), and nuclear import resumes shortly thereafter at 12–13 min (Fig. 8, C and E). Depletion of Greatwall–MASTL accelerates both NUP153 recruitment and nuclear import by ~5 min (Fig. 8, C–E). Conversely, depletion of B55 delayed recruitment of NUP153 by ~5min, and nuclear import was only observed late in telophase at 18–21 min (Fig. 8, C–E). These results explain why removal of the ENSA–Greatwall inhibitory system causes mitotic catastrophe by altering the timing of nuclear pore reformation and function in addition to precocious central spindle formation and cytokinesis (Manchado et al., 2010; Voets and Wolthuis, 2010; Cundell et al., 2013).

The role of the candidate B55 site at S257 on GFP-NUP153 recruitment was then examined. GFP-NUP153 was recruited to chromatin late in anaphase together with other FG-repeat nucleoporins, followed by RanBP2 (Fig. 9 A). An S257A mutant, which cannot be phosphorylated at the B55 site, showed premature recruitment in anaphase and lead to earlier recruitment of other FG-repeat nucleoporins (Fig. 9 B). In contrast, a GFP-NUP153 B55 BPR mutant showed reduced recruitment in anaphase and telophase (Fig. 9 C). Time-lapse imaging showed GFP-NUP153 was recruited to chromatin 8–9 min after anaphase onset, whereas the BPR mutant showed delayed and attenuated recruitment (Fig. 9, D and E). The S257A mutant showed some enlarged punctate foci in interphase cells and accelerated and increased recruitment at early times in anaphase B (Fig. 9, D and E). However, it was not accelerated to the extent seen in Greatwall–MASTL-depleted cells (Fig. 8 B), showing that there are additional B55 substrates acting earlier in nuclear envelope and pore formation. It was not possible to perform quantitative analysis of NUP153 BPR mutant dephosphorylation because attempts to produce a sufficiently sensitive phosphospecific antibody or a unique diagnostic tryptic peptide for mass spectrometry were not successful. These findings on nuclear pore regulation and function and the timing of NUP153 recruitment extend results already obtained for PRC1 and TPX2 to later B55 substrates.
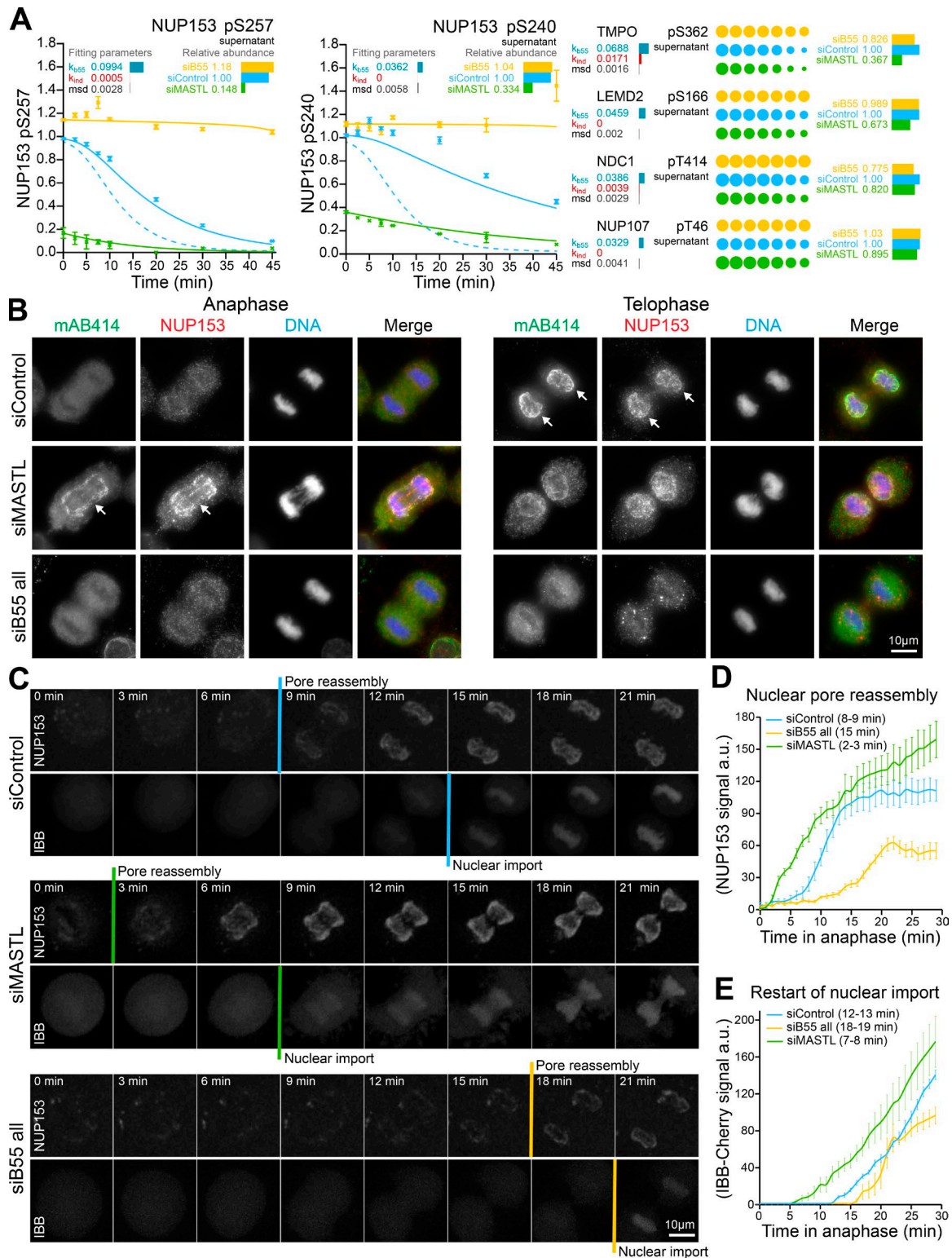
Figure 8. **B55 regulates the timing of nuclear pore reassembly and nuclear transport during mitotic exit.** (A) Nuclear pore proteins identified as candidate B55 substrates. PPSIM plots for NUP153 pS257 and pS240 are shown; the dotted line indicates the profile for PRC1 pT470 and TPX2 pT369. PPSIM kinetic profiles for TMPO pS362, LEMD2 pS166, NDC1 pT414 and NUP107 pT46 are displayed on the right. Error bars indicate the SEM (siControl, n = 5; siB55, n = 3; siMASTL, n = 2). (B) The localization of NUP153 (red) and FG-repeat nucleoporins (mAb414; green) is shown in anaphase and telophase control cells (siControl) and cells depleted of Greatwall (siMASTL) or all B55 regulatory subunits (siB55 all). DNA was stained with DAPI (blue). (C) Reformation of nuclear pores and the resumption of nuclear import were followed by live-cell imaging of cells expressing GFP-NUP153 and the mCherry-Importin β binding domain (IBB), respectively. Images are shown every 3 min from the onset of anaphase (t = 0 min) until 21 min for control cells (siControl) and cells depleted of Greatwall (siMASTL) or all B55 regulatory subunits (siB55 all). (D and E) Nuclear pore reassembly was measured using the GFP-NUP153 signal surrounding the segregating chromatin (D), and nuclear import was defined as the mCherry-IBB signal within this region (E). Error bars indicate SEM (n = 6).
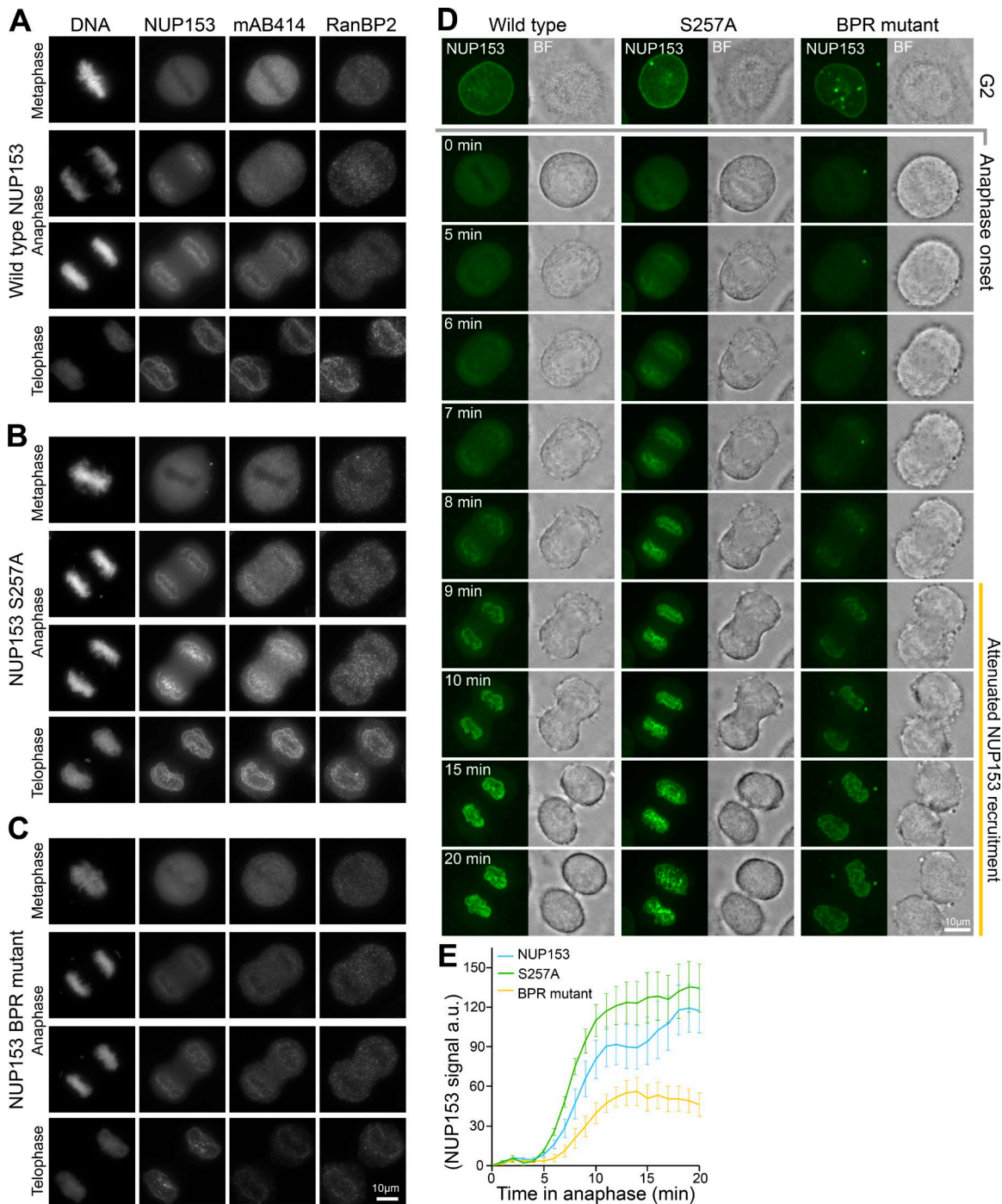
Figure 9.   **A BPR in NUP153 promotes timely activation in anaphase.** (A) The localization of wild-type, (B) S257A, and (C) BPR mutant (R^{214}/K^{227}/K^{228} were mutated to alanine) GFP-NUP153 at different stages of mitosis is shown compared with FG-repeat nucleoporins (mAb414), RanBP2, and DNA. (D) HeLa cells expressing GFP-NUP153 wild-type, S257A, and BPR mutants were imaged every minute through mitosis. Images of G2 cells before mitotic entry, and at the times indicated from the onset of anaphase, are shown. (E) Nuclear pore reassembly was measured using the GFP-NUP153 signal surrounding the segregating chromatin. Error bars indicate SEM (n = 6).

Discussion

An electrostatic code for rate in BEG pathway substrates

In both yeast and mammalian cells, different proteins are dephosphorylated at discrete rates in anaphase. This is thought to be important for timing events during mitotic exit (Malik et al., 2009; Bouchoux and Uhlmann, 2011; McCloy et al., 2015).

However, the mechanisms encoding the specific dephosphorylation rate and timing properties of different substrate proteins have not been elucidated until now. Here, we provide a mechanism that can explain this for the BEG pathway in mammalian cells. B55 substrates have a defined bipartite polybasic motif in which increased numbers of BRs play a cooperative role in determining dephosphorylation rate. This simply explains how a specific dephosphorylation rate can be encoded into a given substrate. As

B55 activity passes a series of thresholds during the transition into anaphase, it will act on progressively less basic substrates. Related mechanisms have been identified previously, most notably the myristoyl-electrostatic switch in which multiphosphorylation regulates membrane binding of MARCKS (McLaughlin and Aderem, 1995) and Ste5 (Serber and Ferrell, 2007; Strickfaden et al., 2007). In the best understood of these systems, phosphorylation modulates a protein interaction with the charged surface of a lipid bilayer (Serber and Ferrell, 2007). Here, we propose that different levels of basic charge in the substrate protein can be used to determine the rate of dephosphorylation by increasing residence time of the substrate at an enzyme surface.

Phospho–amino acid selectivity of PP2A family phosphatases

Mass spectrometry analysis of Cdk1-site turnover in mitotic exit has found that phosphothreonine turns over more rapidly than phosphoserine (Malik et al., 2009; McCloy et al., 2015). In part, this can now be explained by the activity of B55, which shows a preference for phosphothreonine compared with phosphoserine containing substrates. For some substrates tested here (PRC1 and TPX2), threonine appears to be an absolute requirement. Cdc20, previously reported as a B55 substrate and also found here, is phosphorylated at S41 but shows slow dephosphorylation kinetics compared with the threonine-containing substrates PRC1 and TPX2 despite containing a similar BPR sequence. Often overlooked older literature showed that the k_{cat} of PP2A for short phosphothreonine-containing peptide substrates is at least 34-fold higher than for otherwise identical phosphoserine substrates (Deana et al., 1982; Deana and Pinna, 1988; Cohen, 1989). Because these peptide substrates lacked the BPR described here, these authors were measuring basal catalytic activity conferred predominantly by the catalytic subunit. Indeed, these authors initially named this subpopulation of PP2A protein phosphatase-T to reflect its specificity for phosphothreonine.

In this context, it is also interesting to note that the B55 inhibitors ENSA and ARPP19 have a phosphorylated serine in the inhibitory motif that is only very slowly dephosphorylated. The observed k_{cat} is two or three orders of magnitude lower than Cdk-phosphorylated threonine-containing substrates (Williams et al., 2014). The high affinity of phosphorylated ENSA for B55 (K_M of ∼1 nM; Williams et al., 2014) can therefore be explained by a combination of two factors: the saturating number of BRs within the ENSA BPR and its serine phosphorylation by Greatwall. Indeed, Greatwall appears to be highly selective for serine in the ENSA motif, suggesting properties selected for generating a slowly dephosphorylated inhibitor.

In summary, this work provides a unified mechanism for both substrate selection and the feedback control of B55 activity by the phosphoserine-containing substrate/inhibitor ENSA. This explains the complex temporal behavior of cells exiting mitosis, where proteins sharing similar recognition determinants are regulated at widely differing rates by a single pathway. Our data explain how temporal order is encoded by a combination of the B55–ENSA–Greatwall pathway and different strengths of B55 recognition motifs in different classes of substrate protein. Furthermore, we provide a method to define phosphatase substrates using mass spectrometry and identify the molecular motifs underlying substrate recognition and temporal order of dephosphorylation. Using the dataset accompanying this work and variations of the techniques outlined here, it should be possible in the future to dissect mitotic dephosphorylation in its entirety.

Materials and methods

Reagents and antibodies

Antibodies to PRC1, ENSA, KIF4A, and KIF4A pT799 were described previously (Cundell et al., 2013; Nunes Bastos et al., 2013). The commercial antibodies used were PRC1 pT481 (2189–1; Epitomics), cyclin B1 (05–373; EMD Millipore), tubulin (T6199; Sigma-Aldrich), PPP2CA (610555; BD), PPP2R1A (sc-6112; Santa Cruz Biotechnology, Inc.), PPP2R2A (5689S; Cell Signaling Technology), PPP2R5A (A300-967A; Bethyl Laboratories, Inc.), PPP2R5C, (sc-374380; Santa Cruz Biotechnology, Inc.), PPP2R5D (A301-100A; Bethyl Laboratories, Inc.), MASTL (A302-190A; Bethyl Laboratories, Inc.; or ab135637; Abcam), nucleoporin FG-repeat mAb414 (ab24609; Abcam), lamin B receptor (1398–1; Epitomics), AHCTF1 (A300-166A; Bethyl Laboratories, Inc.), NUP153 (A301-788A; Bethyl Laboratories, Inc.), RanBP2 (A301-797A; Bethyl Laboratories, Inc.), FLAG epitope tag (F7425; Sigma-Aldrich). Affinity-purified primary and HRP-coupled secondary antibodies (Jackson ImmunoResearch Laboratories, Inc.) were used at 1 µg/ml final concentration. All Western blots were revealed using ECL (GE Healthcare).

General laboratory chemicals and reagents were obtained from Sigma-Aldrich and Thermo Fisher Scientific unless specifically indicated. Inhibitors were obtained from Sigma-Aldrich (flavopiridol; 5 mM of 1,000× stock), Tocris Bioscience (AZ3146; 20 mM of 1,000× stock), Axon Medchem (BI2536; 1 mM of 1,000× stock), and Enzo Life Sciences (Microcystin-LR; 2 mM of 1,000× stock; Okadaic acid, 500 µM of 250× stock). A benchtop microfuge (5417R; Eppendorf) was used for all centrifugations unless otherwise indicated. For Western blotting, proteins were separated by SDS-PAGE and transferred to nitrocellulose using a Trans-blot Turbo system (Bio-Rad Laboratories). Protein concentrations were measured by Bradford assay using Protein Assay Dye Reagent Concentrate (Bio-Rad Laboratories).

Cell culture procedures

HeLa cells were cultured in growth medium (DMEM containing 10% [vol/vol] bovine calf serum; Invitrogen) at 37°C and 5% CO_2. For synchronization, cells were treated for 18–20 h with 2 mM thymidine, then washed three times in PBS and twice with growth medium. For plasmid and siRNA transfection, Mirus LT1 (Mirus Bio LLC) and Oligofectamine (Invitrogen), respectively, were used according to the manufacturer's instructions. The siRNA duplexes were obtained from GE Healthcare or QIAGEN and have been described already (Cundell et al., 2013).

Dephosphorylation time-course samples for phosphoproteomics

For each condition, 5 × 15–cm dishes were seeded at a density of $6 × 10^5$ cells in 20 ml growth medium, left to adhere for 24 h, and then transfected with siRNA duplexes targeting luciferase (control), PPPR2A-D (B55 regulatory subunits) or MASTL for 54 h. After an additional 18-h treatment with 100 ng/µl nocodazole mitotic cells were washed twice in 50 ml ice cold PBS and once in 1 ml PBS and then split into two 500 µl aliquots. All centrifugation was performed at 200 g_{av}, 5 min at 4°C. One aliquot of cells was harvested and then incubated on ice at 1,500 cells/µl of ice-cold mitotic lysis buffer (50 mM Tris-HCl, pH 7.35, 150 mM NaCl, 1% [vol/vol] IGEPAL, 1 mM DTT, and protease inhibitor cocktail [P8340; Sigma-Aldrich]) supplemented with 2 µM okadaic acid. This represents the 0-min time point. The other aliquot was treated as before but incubated in the absence of phosphatase inhibitors. Samples were removed at 2.5, 5.0, 7.5, 10, 20, 30, and 45 min after addition of ice-cold mitotic lysis buffer and supplemented with 2 µM okadaic acid to stop reactions. After isolation of the last time point, extracts were clarified at 20,000 g_{av} for 15 min at 4°C. Supernatant and chromatin pellet fractions were separated. Western blot samples were isolated and

protein concentrations measured from the supernatant fraction before snap freezing on liquid nitrogen and storage at −80°C.

Digestion of soluble supernatant and chromatin pellet fractions

Supernatant fractions were thawed on ice and protein precipitated using a final concentration of 12.6% (vol/vol) trichloroacetic acid on ice for 1 h before centrifugation at 20,000 g_{av} for 5 min. Precipitated proteins were washed three times with 1 ml acetone, dried for 15 min at room temperature, and then solubilized in 8 M urea. Chromatin pellet fractions were removed from −80°C and resuspended in 50 mM ammonium bicarbonate, 8 M urea buffer. Supernatant and chromatin pellet fractions were reduced using 4 mM DTT (Fluka) for 25 min at 56°C followed by alkylation using 8 mM iodoacetamide incubation in the dark for 30 min. Excess iodoacetamide was quenched by addition of DTT to a final concentration of 8 mM. Proteins were digested first with lysyl endopeptidase (Wako Pure Chemical Industries) for 4 h at 37°C in 8 M urea, then, after dilution to 2 M urea, with 50 mM ammonium bicarbonate, with trypsin (Trypsin Gold; Promega) for 12 h at 37°C. Digestions were quenched by acidification with 5% (vol/vol) formic acid.

Dimethyl labeling and titanium dioxide phosphopeptide enrichment

Tryptic peptides, equivalent to 0.35–2.5 mg of total supernatant protein, were bound to SepPak reverse-phase C18-columns (Waters) and subjected to on-column dimethyl labeling as previously described (Boersema et al., 2009). Peptides from all time points of the dephosphorylation assay were labeled with cyanoborohydride and deuterated formaldehyde to generate a mass increase of 32 D per primary amine, referred to as the heavy label. Additionally, one aliquot of the 0 min time point was labeled with formaldehyde and cyanoborohydride to generate a mass increase of 28 D per primary amine, referred to as the light label. After this, 200 µg light- and heavy-labeled peptides was mixed and then subjected to titanium dioxide enrichment.

Phosphopeptide enrichment was performed using microspin columns packed with titanium dioxide (TopTip; Glygen). All spin steps were performed at 550 rpm, equivalent to 34 g, for 5 min at room temperature. Columns were washed with 65 µl elution buffer (5% ammonia solution in water), then three times with 65 µl loading buffer (5% [vol/vol] trifluoroacetic acid, 1M glycolic acid, 80% [vol/vol] acetonitrile). An equal volume of loading buffer was added to the dimethyl labeled peptide mixtures and then phosphopeptides were bound 65 µl at a time. After binding, columns were washed once each with loading buffer, then with 0.2% (vol/vol) trifluoroacetic acid in 80% (vol/vol) acetonitrile, followed by 20% (vol/vol) acetonitrile. Isotopically coded phosphopeptides were eluted with three washes of 20 µl of elution buffer into 20 µl of 10% (vol/vol) formic acid and 10% (vol/vol) DMSO.

Online nano-LC and tandem mass spectrometry

LC was performed using an EASY-nano-LC 1000 system (Proxeon) in which phosphopeptides were initially trapped on a 75 µm internal diameter guard column packed with Reprosil-Gold 120 C18, 3 µm, 120 Å pores (Dr. Maisch GmbH) in solvent A (0.1% [vol/vol] formic acid in water) using a constant pressure of 500 bar. Peptides were then separated on a 45°C heated EASY-Spray column (50 cm × 75 µm ID, PepMap RSLC C18, 2 µm; Thermo Fisher Scientific) using a 3 h linear 8–30% (vol/vol) acetonitrile gradient and constant 200 nl/min flow rate. Peptides were introduced via an EASY-Spray nano-electrospray ion source into an Orbitrap Elite mass spectrometer (Thermo Fisher Scientific). Spectra were acquired with resolution 30,000, m/z range 350–1,500, AGC target 10^6, maximum injection time 250 ms. The 20 most abundant peaks were fragmented using CID (AGC target 5×10^3, maximum injection time 100 ms) or ETD (AGC cation and anion target 5×10^3 and 2×10^5, respectively, maximum injection time 100 ms, normalized

collision energy 35%) in a data-dependent decision tree method. Peptide identification and quantitation of heavy to light phosphopeptide ratios was then performed using MaxQuant (Cox et al., 2011).

PPSIM analysis

The code used to perform data analysis and modeling is freely available at https://github.com/novakgroupoxford/2016_Cundell_et_al. Time-resolved data on the level of phosphorylation were extracted from MaxQuant data tables containing information on the normalized heavy/light phosphopeptide ratio. Means and standard errors are calculated across the different experimental repeats. Furthermore, we extract the relevant cross-mixing data, information on the gene-name and protein ID of the peptide, as well as information on the position of the phosphosite in the sequence of the protein. To account for potential differences between the behavior of a peptide in the supernatant and in the pellet fraction, they are treated separately.

To reduce the extracted dataset to its fittable subset entries were discarded for: missing data at time point 0, fewer than four time points, missing cross-mixing data relative to control, normalized ratios larger than 10, missing gene name or protein-identifier information. Go-Terms from the Panther database and information of the sequence of the whole protein were then added to the table.

Core model core describing B55 dephosphorylation activity

A wiring diagram for the regulation of B55 activity is shown in Fig. 1 D. Phosphorylated ENSA ($ENSA_p$) in complex with B55 is dephosphorylated at a rate k_{cat}. Complex formation is governed by the association and dissociation rate constants k_{ass} and k_{diss}. Phosphorylated substrates are dephosphorylated in a process independent of B55 (k_{ind}) and in a manner depending on free B55 (k_{b55}). These are described by the following ordinary differential and algebraic equations:

$$\frac{dENSA_{p,total}}{dt} = -k_{cat} \cdot B55{:}ENSA_p,$$

$$\frac{dB55{:}ENSA_p}{dt} = k_{ass} \cdot B55_{free} \cdot ENSA_{p,free} - (k_{diss} + k_{cat}) \cdot B55{:}ENSA_p,$$

$$\frac{dSubstrate_p}{dt} = -(k_{ind} + k_{B55} \cdot B55_{free}) \cdot Substrate_p,$$

$$B55_{free} = B55_{total} - B55{:}ENSA_p,$$

and

$$ENSA_{p,free} = ENSA_{p,total} - B55{:}ENSA_p.$$

The model allows for three distinct states (control, B55 depleted, and Gwl depleted) that are described by informed changes of parameters and initial conditions using experimental data. Initial values for $ENSA_{p,total}$ and $Substrate_p$ are set equal to the corresponding abundance at $t = 0$ in the experimental data, relative to the control condition. To describe the B55-depletion case, an additional parameter, depletion, is introduced to account for the reduced activity of $B55_{total}$.

Time-resolved data for the relative abundance of ENSA phosphorylated on S67 are interpreted to reflect the total pool of phosphorylated ENSA in the system (both free and B55-bound $ENSA_p$). Similarly, the relative abundance of PRC1 phosphorylated on T481 reflect the abundance profile of a well-established substrate of B55. To estimate the activity profile of B55 toward its substrates in a robust manner, time courses for ENSA and PRC1 are considered jointly. Simulations of $ENSA_{p,total}$ and $Substrate_p$ over time ($t = [0, 2.5, 5.0, 7.5, 10,$

20, *30*, *45*]) are compared with the corresponding experiment by calculating the mean square deviation across all conditions (*c* = [*Control*, *B55*, *GWL*]) in both datasets (*d* = [*ENSA*$_{p,total}$, *Substrate*$_p$]):

$$o(P) = \frac{\sum_c \sum_t \sum_d \left[y_{c,t,d}^{data} - y(P)_{c,t,d}^{model} \right]}{2 \cdot \sum_c \sum_t \sum_d (1)}.$$

At the optimal parameter set *P*, the objective function *o*(*P*) becomes minimal. An interior-point algorithm for box-constrained minimization problems was used to find the optimal parameter set.

Modeling substrate dephosphorylation

B55 activity was then used to model substrate dephosphorylation as follows. Integrating the differential equation for Substrate$_p$, $dSubstrate_{p/dp} = -(k_{ind} + k_{B55} \cdot B55_{free}) \cdot Substrate_p$, gives an expression for the abundance of the phosphorylated substrate at a given point in time (*t*) that depends on *t* and the integral of B55 activity between *t* = 0 and *t*:

$$Substrate_p(t) = exp\left[-k_{ind} \cdot t - k_{B55} \cdot \int_0^t B55(t)dt \right].$$

This integral can be approximated by the rectangle method:

$$\int_0^{t_{end}} B55(t)dt \simeq \sum_{i=0}^{t_{end}-1} (t_{i+1} - t_i)B55(t_i).$$

The expression for the abundance of a phosphorylated substrate therefore becomes

$$Substrate_p(t) \simeq exp\left[-k_{ind} \cdot t - k_{B55} \cdot \sum_{i=0}^{t_{end}-1} (t_{i+1} - t_i)B55(t_i) \right].$$

Using this expression and an interior-point algorithm for box-constrained minimization problems, the dataset comprising thousands of temporal profiles for potential B55-dependent substrates can be fitted.

Substrate identification

Candidate B55 substrates were defined as peptides with a quality of fit <0.005 returned by the function *o*(k_{ind}, k_{B55}) and B55-dependent dephosphorylation rate $k_{B55} > 0$, $k_{B55} > $ B55-independent rate k_{ind}, and k_{B55} lie in the top 15th percentile. Likewise, for B55-independent substrates, the quality of fit <0.005 and $k_{ind} > 0$, $k_{ind} > k_{B55}$, and k_{ind} lie in the top 15th percentile.

Electrostatic properties of B55 substrates and dephosphorylation rate

The following form of the Michaelis–Menten equation gives the initial rate of dephosphorylation at one relative unit substrate concentration, where the values of both V_{max} and K_M are normalized to the initial substrate concentration:

$$V_{dp} = \frac{V_{max}}{1 + K_M}.$$

BRs in the substrate reduce the dissociation constant (k_{dis}) of the B55–substrate complex in a cooperative fashion. This effect can be described by the Arrhenius equation, assuming that the activation energy of dissociation (E_a) is proportional to the number of BRs in the substrate. This assumption allows us to divide K_M into a constant and a BR-dependent term:

$$V_{dp} = k'_{dp} + \frac{V_{max}}{1 + K'_M + K_D^{BR} \cdot e^{\frac{-E_a \cdot BR}{RT}}} \qquad (1)$$

$$K'_M = \frac{k_{cat} + k'_{dis}}{k_{ass}}$$

is determined by a BR-independent dissociation rate constant: (k'_{dis}), whereas

$$K_D^{BR} = \frac{k_{dis}^{BR}}{k_{ass}}$$

is the maximal equilibrium dissociation constant in the absence of any BRs. We also supplement the rate expression by a small and constant dephosphorylation rate independent from B55 (k'_{dp}). Eq. 1 defines V_{dp} as a sigmoid function as a function of BRs. Eq. 1 was fitted to the experimentally estimated initial dephosphorylation rates of PRC1 and ENSA using the Excel Solver package (Microsoft) with E_a = 2.5 kJ mol^{-1}, R = 8.314 kJ mol^{-1} K^{-1} and T = 277 K (4°C). Estimated parameter values are PRC1 V_{max} = 0.425 min^{-1}, K'_M = 4, K_D^{BR} = 300, k'_{dp} = 0.007 min^{-1}, ENSA V_{max} = 0.14 min^{-1}, K'_M = 0.01, K_D^{BR} = 1,000, and k'_{dp} = 0.015 min^{-1}.

The temporal pattern of PRC1 dephosphorylation (Fig. 3 F) was approximated by numerical integration, between relative concentrations of one and zero, of

$$-\frac{d[PRC1]}{dt} = k'_{dp} \cdot [PRC1] + \frac{V_{max} \cdot [PRC1]}{[PRC1] + K'_M + K_D^{BR} \cdot e^{\frac{-E_a \cdot BR}{RT}}}$$

Because of the tight binding of ENSA to B55, the total quasi–steady-state approximation (Williams et al., 2014; Vinod and Novak, 2015) is used to calculate pENSA dephosphorylation kinetics (Fig. 6 F):

$$-\frac{d[pENSA]_T}{dt} = \frac{V_{max}}{[B55]_T} \cdot \frac{\beta - \sqrt{\beta^2 - 4[pENSA]_T[B55]_T}}{2},$$

where β = $[pENSA]_T + [B55]_T + K_M^{B55}$, $[pENSA]_T$ = 1, and $[B55]_T$ = 0.25, and where pENSA$_T$ is the sum of free (pENSA) and PP2A-B55 complexed (pENSA–B55) forms of phosphorylated ENSA.

Purification of PP2A holoenzymes for phosphatase assays

HEK293T cells were seeded onto 15-cm dishes (7.5 × 10^6 cells per dish) and grown for 24 h. Six dishes per condition were transiently transfected with 2 µg pCDNA5-FLAG (empty vector control), pCDNA5-FLAG-PPP2R2A (B55α), pCDNA5-FLAG-PPP2R2A-DE/A mutant, or pCDNA5-FLAG-PPP2R5C (B56γ). After harvesting, cells were washed three times in 50 ml ice-cold PBS, centrifuged at 400 *g*, 3 min, 4°C, and then pellets lysed in 2 ml ice-cold T-lysis buffer (20 mM Tris-HCl, pH 7.35, 150 mM NaCl, 1% [vol/vol] Triton-X 100, and protease inhibitor cocktail; Sigma-Aldrich) on ice for 15 min. Extracts were clarified at 20,817 g_{av} for 15 min at 4°C, supernatants were isolated, and 200 µl of FLAG M2-agarose beads (Sigma-Aldrich) prewashed in T-lysis buffer was added per condition. After 3 h at 4°C, beads were washed two times in T-lysis buffer, four times in TBS (20 mM Tris-HCl, pH 7.35, and 150 mM NaCl) containing 0.1% (vol/vol) Triton-X 100, one time in TBS, and one time in elution buffer (20 mM Tris-HCl, pH 7.35, 150 mM NaCl, and 1 mM MnCl$_2$). Bound proteins were eluted from beads in 200 µl elution buffer containing 200 µg/ml FLAG peptide (F3290; Sigma-Aldrich) at 4°C for 30 min. Glycerol and DTT were added to the eluate to final concentrations of 25% (vol/vol) and 1 mM, respectively, before freezing.

Substrate dephosphorylation assays

Dephosphorylation reactions were set up on ice and performed in tubes treated with a blocking buffer (50 mM Tris, pH 7.35, 150 mM NaCl, 0.1 mM MnCl$_2$, 1 mM MgCl$_2$, 1 mM DTT, 0.1% [vol/vol] IGEPAL, and 2 mg/ml BSA) to limit nonspecific loss of protein components on tube walls. Cdk1-phosphorylated PRC1 was produced as described previously (Cundell et al., 2013; Bastos et al., 2014). Assays used 100–180 ng B55α or B56γ holoenzyme and 600–1,333 ng substrate

protein in 175 µl reaction buffer (50 mM Tris, pH 7.35, 150 mM NaCl, 0.1 mM $MnCl_2$, 1 mM $MgCl_2$, 1 mM DTT, 0.1% [vol/vol] IGEPAL, 0.2 mg/ml BSA, 5 µM flavopiridol, and 1 µM BI2536). An equal volume of undiluted eluate from the pCDNA5-FLAG (empty vector) control immunoprecipitate was used in mock reactions to ensure that nonspecific phosphatase activity was not associated with the beads. Samples were taken at indicated time points and dephosphorylation was stopped by addition of 2 µM microcystin-LR. Samples were then processed for proteomic analysis or Western blotting. For specific detection of the MASTL phosphorylated form of ENSA, resolving gel buffer was supplemented with 12.5 µM Phos-tag (NARD Chemicals) and 100 µM $MnCl_2$ as described previously (Cundell et al., 2013). ENSA phosphorylated at S67 can be resolved from other phosphorylated forms of ENSA by this procedure (Mochida, 2014).

Live- and fixed-cell microscopy

Fixed-cell microscopy was performed as described previously (Bastos et al., 2014). Secondary antibodies conjugated to Alexa Fluor 488, 555, and 647 were obtained from Invitrogen. DNA was stained with DAPI (Sigma-Aldrich). For live-cell imaging, cells were plated in 35-mm dishes with a 14-mm No. 1.5 thickness coverglass window (MatTek Corporation) then treated as described in the figure legends. The dishes were placed in a 37°C and 5% CO_2 environment chamber (Tokai Hit) on an inverted microscope (IX81; Olympus) with a 60× 1.42 NA oil-immersion objective coupled to an Ultraview Vox spinning disk confocal system running Volicity 6 (PerkinElmer). Images were captured with a EM-CCD camera (C9100-13; Hamamatsu Photonics). Exposure times were 50 ms at 4% 488-nm laser power for GFP-PRC1 constructs, 100 ms at 8% 488-nm laser power for GFP-NUP153, and 20 ms at 2% 561-nm laser power for mCherry-IBB. Image stacks of 16–18 planes spaced 0.6 µm apart were taken at one to four stage positions every minute as cells passed through mitosis. A brightfield reference image was taken to visualize cell shape using 100-ms exposure. Volume-based quantitations of PRC1 levels at the spindle midzone were measured by integrating the intensity at the cell equator and midbody region for the full four-dimensional dataset (xyz space, time) for 20 min after anaphase onset using the quantitation tools in Volicity 6. The same approach was used to measure NUP153 and IBB levels over the nucleus. Images for figures and movies in 24-bit RGB or 8-bit grayscale TIFF format were created using maximum intensity projection of the fluorescent channels. Images were then placed into Adobe Illustrator and text labels added to produce the figures.

Online supplemental material

Fig. S1 shows a proteomic strategy for the identification of B55 substrates. Fig. S2 shows mapping the B55 recognition determinant in PRC1. Fig. S3 shows BPRs control timing of PRC1 and TPX2 localization to the anaphase spindle. Fig. S4 shows purification of wild-type and acidic surface mutant B55α. Fig. S5 shows B55 regulates the timing of nuclear pore reassembly. Supplemental data tables contain the mass spectrometry dataset showing dephosphorylation kinetics, B55-dependent and independent substrates, and mitotic proteome. Online supplemental material is available at http://www.jcb.org/cgi/content/full/jcb.201606033/DC1.

References

Alexander, J., D. Lim, B.A. Joughin, B. Hegemann, J.R. Hutchins, T. Ehrenberger, F. Ivins, F. Sessa, O. Hudecz, E.A. Nigg, et al. 2011. Spatial exclusivity combined with positive and negative selection of phosphorylation motifs is the basis for context-dependent mitotic signaling. *Sci. Signal.* 4:ra42. http://dx.doi.org/10.1126/scisignal.2001796

Bastos, R.N., M.J. Cundell, and F.A. Barr. 2014. KIF4A and PP2A-B56 form a spatially restricted feedback loop opposing Aurora B at the anaphase central spindle. *J. Cell Biol.* 207:683–693. http://dx.doi.org/10.1083/jcb.201409129

Boersema, P.J., R. Raijmakers, S. Lemeer, S. Mohammed, and A.J. Heck. 2009. Multiplex peptide stable isotope dimethyl labeling for quantitative proteomics. *Nat. Protoc.* 4:484–494. http://dx.doi.org/10.1038/nprot.2009.21

Bouchoux, C., and F. Uhlmann. 2011. A quantitative model for ordered Cdk substrate dephosphorylation during mitotic exit. *Cell.* 147:803–814. http://dx.doi.org/10.1016/j.cell.2011.09.047

Castilho, P.V., B.C. Williams, S. Mochida, Y. Zhao, and M.L. Goldberg. 2009. The M phase kinase Greatwall (Gwl) promotes inactivation of PP2A/B55delta, a phosphatase directed against CDK phosphosites. *Mol. Biol. Cell.* 20:4777–4789. http://dx.doi.org/10.1091/mbc.E09-07-0643

Cohen, P. 1989. The structure and regulation of protein phosphatases. *Annu. Rev. Biochem.* 58:453–508. http://dx.doi.org/10.1146/annurev.bi.58.070189.002321

Colaert, N., K. Helsens, L. Martens, J. Vandekerckhove, and K. Gevaert. 2009. Improved visualization of protein consensus sequences by iceLogo. *Nat. Methods.* 6:786–787. http://dx.doi.org/10.1038/nmeth1109-786

Cox, J., N. Neuhauser, A. Michalski, R.A. Scheltema, J.V. Olsen, and M. Mann. 2011. Andromeda: a peptide search engine integrated into the MaxQuant environment. *J. Proteome Res.* 10:1794–1805. http://dx.doi.org/10.1021/pr101065j

Cundell, M.J., R.N. Bastos, T. Zhang, J. Holder, U. Gruneberg, B. Novak, and F.A. Barr. 2013. The BEG (PP2A-B55/ENSA/Greatwall) pathway ensures cytokinesis follows chromosome separation. *Mol. Cell.* 52:393–405. http://dx.doi.org/10.1016/j.molcel.2013.09.005

Deana, A.D., and L.A. Pinna. 1988. Identification of pseudo 'phosphothreonyl-specific' protein phosphatase T with a fraction of polycation-stimulated protein phosphatase 2A. *Biochim. Biophys. Acta.* 968:179–185. http://dx.doi.org/10.1016/0167-4889(88)90006-7

Deana, A.D., F. Marchiori, F. Meggio, and L.A. Pinna. 1982. Dephosphorylation of synthetic phosphopeptides by protein phosphatase-T, a phosphothreonyl protein phosphatase. *J. Biol. Chem.* 257:8565–8568.

Ferrell, J.E. Jr. 2013. Feedback loops and reciprocal regulation: recurring motifs in the systems biology of the cell cycle. *Curr. Opin. Cell Biol.* 25:676–686. http://dx.doi.org/10.1016/j.ceb.2013.07.007

Gharbi-Ayachi, A., J.C. Labbé, A. Burgess, S. Vigneron, J.M. Strub, E. Brioudes, A. Van-Dorsselaer, A. Castro, and T. Lorca. 2010. The substrate of Greatwall kinase, Arpp19, controls mitosis by inhibiting protein phosphatase 2A. *Science.* 330:1673–1677. http://dx.doi.org/10.1126/science.1197048

Glover, D.M. 2012. The overlooked greatwall: a new perspective on mitotic control. *Open Biol.* 2:120023. http://dx.doi.org/10.1098/rsob.120023

Grallert, A., E. Boke, A. Hagting, B. Hodgson, Y. Connolly, J.R. Griffiths, D.L. Smith, J. Pines, and I.M. Hagan. 2015. A PP1-PP2A phosphatase relay controls mitotic progression. *Nature.* 517:94–98. http://dx.doi.org/10.1038/nature14019

Heim, A., A. Konietzny, and T.U. Mayer. 2015. Protein phosphatase 1 is essential for Greatwall inactivation at mitotic exit. *EMBO Rep.* 16:1501–1510. http://dx.doi.org/10.15252/embr.201540876

Kettenbach, A.N., D.K. Schweppe, B.K. Faherty, D. Pechenick, A.A. Pletnev, and S.A. Gerber. 2011. Quantitative phosphoproteomics identifies

substrates and functional modules of Aurora and Polo-like kinase activities in mitotic cells. *Sci. Signal.* 4:rs5. http://dx.doi.org/10.1126/scisignal.2001497

Lowe, M., N.K. Gonatas, and G. Warren. 2000. The mitotic phosphorylation cycle of the cis-Golgi matrix protein GM130. *J. Cell Biol.* 149:341–356. http://dx.doi.org/10.1083/jcb.149.2.341

Malik, R., R. Lenobel, A. Santamaria, A. Ries, E.A. Nigg, and R. Körner. 2009. Quantitative analysis of the human spindle phosphoproteome at distinct mitotic stages. *J. Proteome Res.* 8:4553–4563. http://dx.doi.org/10.1021/pr9003773

Manchado, E., M. Guillamot, G. de Cárcer, M. Eguren, M. Trickey, I. García-Higuera, S. Moreno, H. Yamano, M. Cañamero, and M. Malumbres. 2010. Targeting mitotic exit leads to tumor regression in vivo: Modulation by Cdk1, Mastl, and the PP2A/B55α,δ phosphatase. *Cancer Cell.* 18:641–654. http://dx.doi.org/10.1016/j.ccr.2010.10.028

McCloy, R.A., B.L. Parker, S. Rogers, R. Chaudhuri, V. Gayevskiy, N.J. Hoffman, N. Ali, D.N. Watkins, R.J. Daly, D.E. James, et al. 2015. Global phosphoproteomic mapping of early mitotic exit in human cells identifies novel substrate dephosphorylation motifs. *Mol. Cell. Proteomics.* 14:2194–2212. http://dx.doi.org/10.1074/mcp.M114.046938

McLaughlin, S., and A. Aderem. 1995. The myristoyl-electrostatic switch: a modulator of reversible protein-membrane interactions. *Trends Biochem. Sci.* 20:272–276. http://dx.doi.org/10.1016/S0968-0004(00)89042-8

Mochida, S. 2014. Regulation of α-endosulfine, an inhibitor of protein phosphatase 2A, by multisite phosphorylation. *FEBS J.* 281:1159–1169. http://dx.doi.org/10.1111/febs.12685

Mochida, S., and T. Hunt. 2012. Protein phosphatases and their regulation in the control of mitosis. *EMBO Rep.* 13:197–203. http://dx.doi.org/10.1038/embor.2011.263

Mochida, S., S.L. Maslen, M. Skehel, and T. Hunt. 2010. Greatwall phosphorylates an inhibitor of protein phosphatase 2A that is essential for mitosis. *Science.* 330:1670–1673. http://dx.doi.org/10.1126/science.1195689

Neef, R., U. Gruneberg, R. Kopajtich, X. Li, E.A. Nigg, H. Sillje, and F.A. Barr. 2007. Choice of Plk1 docking partners during mitosis and cytokinesis is controlled by the activation state of Cdk1. *Nat. Cell Biol.* 9:436–444. http://dx.doi.org/10.1038/ncb1557

Novak, B., O. Kapuy, M.R. Domingo-Sananes, and J.J. Tyson. 2010. Regulated protein kinases and phosphatases in cell cycle decisions. *Curr. Opin. Cell Biol.* 22:801–808. http://dx.doi.org/10.1016/j.ceb.2010.07.001

Nunes Bastos, R., S.R. Gandhi, R.D. Baron, U. Gruneberg, E.A. Nigg, and F.A. Barr. 2013. Aurora B suppresses microtubule dynamics and limits central spindle size by locally activating KIF4A. *J. Cell Biol.* 202:605–621. http://dx.doi.org/10.1083/jcb.201301094

Qian, J., M. Beullens, J. Huang, S. De Munter, B. Lesage, and M. Bollen. 2015. Cdk1 orders mitotic events through coordination of a chromosome-associated phosphatase switch. *Nat. Commun.* 6:10215. http://dx.doi.org/10.1038/ncomms10215

Rangone, H., E. Wegel, M.K. Gatt, E. Yeung, A. Flowers, J. Debski, M. Dadlez, V. Janssens, A.T. Carpenter, and D.M. Glover. 2011. Suppression of scant identifies Endos as a substrate of greatwall kinase and a negative regulator of protein phosphatase 2A in mitosis. *PLoS Genet.* 7:e1002225. http://dx.doi.org/10.1371/journal.pgen.1002225

Schatz, C.A., R. Santarella, A. Hoenger, E. Karsenti, I.W. Mattaj, O.J. Gruss, and R.E. Carazo-Salas. 2003. Importin alpha-regulated nucleation of microtubules by TPX2. *EMBO J.* 22:2060–2070. http://dx.doi.org/10.1093/emboj/cdg195

Schmitz, M.H., M. Held, V. Janssens, J.R. Hutchins, O. Hudecz, E. Ivanova, J. Goris, L. Trinkle-Mulcahy, A.I. Lamond, I. Poser, et al. 2010. Live-cell imaging RNAi screen identifies PP2A-B55alpha and importin-beta1 as key mitotic exit regulators in human cells. *Nat. Cell Biol.* 12:886–893. http://dx.doi.org/10.1038/ncb2092

Serber, Z., and J.E. Ferrell Jr. 2007. Tuning bulk electrostatics to regulate protein function. *Cell.* 128:441–444. http://dx.doi.org/10.1016/j.cell.2007.01.018

Strickfaden, S.C., M.J. Winters, G. Ben-Ari, R.E. Lamson, M. Tyers, and P.M. Pryciak. 2007. A mechanism for cell-cycle regulation of MAP kinase signaling in a yeast differentiation pathway. *Cell.* 128:519–531. http://dx.doi.org/10.1016/j.cell.2006.12.032

Subramanian, R., E.M. Wilson-Kubalek, C.P. Arthur, M.J. Bick, E.A. Campbell, S.A. Darst, R.A. Milligan, and T.M. Kapoor. 2010. Insights into antiparallel microtubule crosslinking by PRC1, a conserved nonmotor microtubule binding protein. *Cell.* 142:433–443. http://dx.doi.org/10.1016/j.cell.2010.07.012

Subramanian, R., S.C. Ti, L. Tan, S.A. Darst, and T.M. Kapoor. 2013. Marking and measuring single microtubules by PRC1 and kinesin-4. *Cell.* 154:377–390. (published erratum appears in *Cell.* 2013. 155:1188–1991) http://dx.doi.org/10.1016/j.cell.2013.06.021

Vagnarelli, P., S. Ribeiro, L. Sennels, L. Sanchez-Pulido, F. de Lima Alves, T. Verheyen, D.A. Kelly, C.P. Ponting, J. Rappsilber, and W.C. Earnshaw. 2011. Repo-Man coordinates chromosomal reorganization with nuclear envelope reassembly during mitotic exit. *Dev. Cell.* 21:328–342. http://dx.doi.org/10.1016/j.devcel.2011.06.020

Vinod, P.K., and B. Novak. 2015. Model scenarios for switch-like mitotic transitions. *FEBS Lett.* 589:667–671. http://dx.doi.org/10.1016/j.febslet.2015.02.007

Voets, E., and R.M. Wolthuis. 2010. MASTL is the human orthologue of Greatwall kinase that facilitates mitotic entry, anaphase and cytokinesis. *Cell Cycle.* 9:3591–3601. http://dx.doi.org/10.4161/cc.9.17.12832

Wandke, C., and U. Kutay. 2013. Enclosing chromatin: reassembly of the nucleus after open mitosis. *Cell.* 152:1222–1225. http://dx.doi.org/10.1016/j.cell.2013.02.046

Williams, B.C., J.J. Filter, K.A. Blake-Hodek, B.E. Wadzinski, N.J. Fuda, D. Shalloway, and M.L. Goldberg. 2014. Greatwall-phosphorylated Endosulfine is both an inhibitor and a substrate of PP2A-B55 heterotrimers. *eLife.* 3:e01695. http://dx.doi.org/10.7554/eLife.01695

Wittmann, T., M. Wilm, E. Karsenti, and I. Vernos. 2000. TPX2, A novel *Xenopus* MAP involved in spindle pole organization. *J. Cell Biol.* 149:1405–1418. http://dx.doi.org/10.1083/jcb.149.7.1405

Wurzenberger, C., and D.W. Gerlich. 2011. Phosphatases: providing safe passage through mitotic exit. *Nat. Rev. Mol. Cell Biol.* 12:469–482. http://dx.doi.org/10.1038/nrm3149

Xu, Y., Y. Chen, P. Zhang, P.D. Jeffrey, and Y. Shi. 2008. Structure of a protein phosphatase 2A holoenzyme: insights into B55-mediated Tau dephosphorylation. *Mol. Cell.* 31:873–885. http://dx.doi.org/10.1016/j.molcel.2008.08.006